Influences of ice-water mixture on the vertical water-entry of a cylinder at a low velocity

Hao Wang [a], Yuchuan Luo [b], Zhihua Chen [a], Zeqing Guo [a], Zhengui Huang [a,*]

[a] *National Key Laboratory of Transient Physics, Nanjing University of Science and Technology, Nanjing, 210094, China*
[b] *Xi'an Aerospace Power Measurement and Control Technology Research Institute, Xi'an, Shanxi, 710025, China*

A B S T R A C T

The ice floating on water surfaces during winter significantly influences the water entry process of a cylinder. Therefore, it is crucial to evaluate the influence mechanism of the ice-water mixture during the water entry process. In this study, we used computational fluid dynamics (CFD) to simulate the process of a cylinder vertically entering the water (without floating ice) and ice-water mixture at a low speed based on the finite volume method (FVM), the volume of fluid (VOF) method, the continuum surface force (CSF) model and the overlap grid technology. Results showed that the initial splash shape had changed owing to the floating ice, leading to the absence of the surface closure of the cavity, resulting in a pressure difference change inside and outside the cavity. This significantly influences the characteristics of flow fields, hydrodynamic and motion characteristics of the cylinder. While the motion characteristics of the cylinder were not significantly affected by the thickness of the floating ice, the difference can be seen clearly compared with the case without floating ice. The results of this study can provide a beneficial reference for designing new cross-medium projectiles under extremely low temperature environments during winter.

1. Introduction

The Arctic is an ice-covered treasure, comprising oil reserves that account for approximately 13% of the global oil reserves. Owing to global warming, polar glaciers are gradually melting, and large areas of ice and snow layers have melted into ice-water mixture (LI, 2009; Nam et al., 2013). As a result, the difficulty of Arctic development has also decreased. Countries worldwide, especially in the northern regions, have noted the potential of the Arctic towards economic and commercial benefits, which have become inevitable for the development of the Arctic. Furthermore, because the Bohai Sea and the Yellow Sea, known as the maritime gateways of important cities, have different degrees of sea ice formation in winter every year (Chen and Chen, 2021), it is indispensable to consider the extreme climate combat environment that weapons and equipment face during maritime winter. From the military perspective, alongside the influence of wind, waves, and airflow, the effect of ice-water mixture on the projectile should be considered. Therefore, it is particularly crucial to investigate the influence of ice-water mixture on the vertical entry process of a cylinder at a low speed.

The water entry of objects refers to the three-phase coupling of gas,

liquids, and solids, having strong unsteady characteristics. Worthington and Cole (1897) used a single-flash camera to observe the process of the rigid sphere entering the water at a vertical low speed and analysed the influence of different initial water entering speeds on the cavity diameter and surface splash, which went on to create a new era in the study of water entering problems. The principle of independence of the cavity section expansion, proposed by Logvinovich (1969), is based on the potential flow theory and is the first systematic theory for predicting the expansion form of the cavity, which reflects the supercavitation flow characteristics of a slender body. This theory states that the subsequent development of the cavity section is only associated with the conditions at the birth time of the section and has nothing to do with the conditions before or after. Scolan and Korobkin (2001) and Korobkin and Scolan (2006) studied the hydrodynamic characteristics of blunt bodies entering the water to provide a way of thinking for improving the mathematical model of liquid flow and dynamic characteristics of three-dimensional objects entering the water. Owing to the rapid development of high-speed photography and computer technologies, research on water entry has been deepened, and an increasing number of scholars begin to pour attention into the details of cavities under complex water entry conditions. Gekle et al. (2009, 2010) conducted an

---

experimental investigation on gas flow in the cavity during the necking and deep-closure processes of cavity after the disc impacted the water surface. Results showed that the gas flow speed in the cavity increases rapidly as the cross-sectional area of the cavity decreases during necking and deep-closure of the low-speed water entry cavity process.

The investigations on water entry of the more complicated bodies were increased rapidly at the different initial conditions as the investigation deepened. Truscott and Techet (2009) and Techet and Truscott (2011) analysed the evolution of the cavity shape and the motion characteristics of the sphere under different angular velocities of rotation and carried out experimental research on the water entry of hydrophilic and hydrophobic spheres with different initial rotational speeds using high-speed photography. Truscott et al. (2014) comprehensively summarised similar theories, experimental results, and numerical analysis acquired by different scholars on the water entry of objects. He et al. (2012a, 2012b) conducted several experiments on 140° cone-angle head cylinders with different water entry speeds and angles under the conditions of single, series and parallel, and clarified the similarities and differences of flow phenomena such as cavity generation, development and closure under various conditions. Ma et al. (2014) performed a series of related experiments on spheres entering the water at different speeds and surface wetness degrees. The influence of water entry speed and surface wetness state on the formation of cavities and sphere motion characteristics was obtained. The water entry experiment of a disc cavitator was carried out by Jiang et al. (2017) to investigate its cavity flow characteristics. Wang et al. (2017) analysed the evolution of cavity shape during the low-speed water entry of projectiles with different head shapes. Five types of cavity closure modes, corresponding to different water entry speeds, were summarized, which showed that different head shapes had different effects on cavity size, closure mode, and cavity stability. Huang et al. (2018) investigated the vertical water entry of a 90° and a 60° conical head projectile and a truncated conical head projectile, respectively (Luo et al., 2019), and obtained the influence law of projectile head diameter on the ballistic characteristics.

However, flow field structure characteristics such as velocity distribution and pressure distribution cannot be observed through experimental investigation. Owing to the development of computer science and technology, numerical simulations have become crucial for investigating the water entry problem. Iranmanesh and Passandideh-Fard (2017) established a new three-dimensional numerical calculation model and conducted a numerical simulation investigation on the horizontal water entry of a cylinder at low Froude numbers. The method was verified by comparing with the experiment results, and the influence of water entry parameters such as the cylinder length, diameter, and impact velocity on the cavity shape was expounded. Liu et al. (2020) numerically calculated the oblique water entry of a cylinder with different velocities based on the VOF method. Results showed that as the initial velocity of water entry increases, secondary closure of cavities occurs. An efficient free surface solver for modelling ricochet problems (Nguyen et al., 2020) was used to calculate the water entry process of cylinders with different densities and inclination angles by Nguyen et al. (2021). Results indicated that the angle of entering the water and the density of cylinders significantly influence the motion characteristics of cylinders after entering the water.

The above published literature shows that most studies on water entry problems focus on the object structure and water entry angle, which are dominated by the pure water environment, and do not consider the complex water entry environment where other solids exist. Owing to the upsurge of Arctic development and the strong military demand for combat environments during the ice-up period in the Bohai Sea and the Yellow Sea, the development of underwater attack weapons under extremely low temperature environments has become increasingly crucial. Therefore, it is necessary to investigate the evolution mechanism of the cavity and the motion characteristics of the cylinder in the process of passing through ice-water mixture. The ice-water mixture changes the external environment when entering the water, which makes the process of the cylinder crossing from air to underwater more complicated. However, there is almost no study that investigates the objects crossing the ice-water mixture. Only a few scholars have conducted numerical simulation research on the process of a slender body passing through ice-water mixture from underwater using dynamic software, it was found that the influence degree of different ice distribution patterns and the initial relative positions on the centroid displacement of the slender body and flow field characteristics are different (Zhang et al., 2020; Cai et al., 2020).

In this study, we numerically simulated the process of a cylinder vertically entering the water (without floating ice) at a low speed and passing through ice-water mixture vertically without collision using the finite volume method (FVM) and volume of fluid (VOF) method, continuum surface force (CSF) model and the dynamic fluid body interaction (DFBI) module combined with the overlapping grid technology. Through simulation, we studied the influence law of floating ice on the evolution of the cavity shape, structural characteristics of flow fields, cylinder motion, and fluid hydrodynamic characteristics variation. We believe the results of this study can provide a beneficial reference for designing new cross-medium projectiles under extremely low temperature environments during winter.

2. Numerical methodology

2.1. Governing equations

Assuming the water is incompressible and neglecting the heat conduction effect caused by motion, the field structure and fluid dynamics of multiphase flow are obtained only by solving the mass conservation equation and momentum conservation equation.

Mass conservation is given as:

$$\frac{\partial \rho_m}{\partial t} + \frac{\partial}{\partial x_i}(\rho_m u_i) = 0 \tag{1}$$

$$\rho_m = \rho_g \alpha_g + \rho_l \alpha_l \tag{2}$$

where ρ_m, ρ_g and ρ_l are the mixture, air and water densities, respectively, and u_i is the velocity component of fluid velocity vector in the Cartesian coordinate system. α_g and α_l are the volume fractions of air and water, respectively.

Momentum conservation equation is given as:

$$\frac{\partial(\rho_m u_i)}{\partial t} + \frac{\partial(\rho_m u_i u_j)}{\partial x_j} = -\frac{\partial P}{\partial x_i} + \mu_m \frac{\partial}{\partial x_j}\left(\frac{\partial u_i}{\partial x_j} + \frac{\partial u_j}{\partial x_i}\right) + \rho_m g_i \tag{3}$$

where μ_m is the dynamic viscosity of the mixed medium, P is the flow field pressure, ε and k are the turbulent dissipation rate and kinetic energy, respectively.

Only air-water two-phase flow is involved in the low-speed water entry that means no phase change occurs. The volume fraction of each phase is used to describe the percentage of different fluids in the process of water entry. α_l and α_g represent water and air, respectively, where the main phase is liquid, and the existence of fluid or gas in the volume element is distinguished depending on the volume fraction value:

$\alpha_l = 0$——The volume element is completely filled with air phase instead of water phase

$\alpha_l = 1$——The volume element is completely filled with water phase instead of air phase

$0 < \alpha_l < 1$——The volume element comprises both water and air phases

Flow follows the law of conservation of components, given as:

$$\alpha_l + \alpha_g = 1 \tag{4}$$

2.2. Turbulent model

The SST k-ω two-equation turbulence model was used to solve the fluid governing equation, considering the SST k-ω two-equation turbulence model (Menter, 1993) combined with the wall function considers the transport problem of turbulent shear force, and can better describe the turbulent flow. Furthermore, it exhibits higher accuracy in predicting the encircling and swirling flow near the wall. The transport equation is given as:

$$\frac{\partial(\rho_m k)}{\partial t} + \frac{\partial(\rho_m k u_j)}{\partial x_j} = \frac{\partial}{\partial x_j}\left[\left(\mu + \frac{\mu_t}{\sigma_k}\right)\frac{\partial k}{\partial x_j}\right] + \widetilde{G}_k - Y_k + S_k \quad (5)$$

$$\frac{\partial(\rho_m \omega)}{\partial t} + \frac{\partial(\rho_m \omega u_j)}{\partial x_j} = \frac{\partial}{\partial x_j}\left[\left(\mu + \frac{\mu_t}{\sigma_\omega}\right)\frac{\partial \omega}{\partial x_j}\right] + G_\omega - Y_\omega + S_\omega + D_\omega \quad (6)$$

where $\mu_t = \rho m k T$ is the turbulent dynamic viscosity, T is the turbulent time scale, $\widetilde{G}_k$ is the turbulent kinetic energy generated by the average velocity gradient, Y_k is the turbulent energy dissipation, Y_ω is the dissipation term of a specific dissipation rate, S_k and S_ω are the user-specific source items, ω is the turbulent dissipation rate, G_ω is the turbulent kinetic energy velocity gradient, D_ω is the cross-diffusion term, and σ_k and σ_ω are the Prandtl constants of turbulence.

2.3. Motion equation of six degrees of freedom body

The DFBI module was used to establish an unconstrained six degrees of freedom (6-DOF) body including translation and rotation in three directions, to accurately describe the motion of the cylinder and floating ice. Furthermore, DFBI can simulate the motion of a rigid body caused by fluid forces at the coupling boundary, as well as the forces and moments applied by additional user-defined parts.

Considering the centroid position and deflection angle of the moving body at the last moment are known, the translation and angular velocities of the moving body are calculated according to the centroid translation and body rotation equations. After recalculation, the centroid position and deflection angle at the next moment can be obtained.

The centroid translation equation defined by the global inertial coordinate system is given as:

$$m\frac{d\boldsymbol{u}}{dt} = \boldsymbol{f} \quad (7)$$

where m is body mass, $\boldsymbol{u}$ is the velocity vector of the centre of mass at time t, $\boldsymbol{f}$ is the combined force acting on the body, including fluid forces and gravity, which is defined as:

$$\boldsymbol{f} = \boldsymbol{fp} + \boldsymbol{f\tau} + mg \quad (8)$$

where $\boldsymbol{fp}$ is the fluid pressure acting on the body and $\boldsymbol{f\tau}$ is the fluid shear force acting on the body, which can be obtained by integrating the fluid pressure force and shear force acting on the surface of the body, respectively.

The body rotation equation, based on the local coordinate system with the origin as the centroid, is given as:

$$\boldsymbol{J}\frac{d\boldsymbol{\omega}}{dt} + \boldsymbol{\omega} \times \left(\boldsymbol{J} \bullet \boldsymbol{\omega}\right) = \boldsymbol{M} \quad (9)$$

where $\boldsymbol{J}$ and $\boldsymbol{\omega}$ are the moment of inertia tensor and angular velocity of the body, respectively, and $\boldsymbol{M}$ is the resultant moment acting on the centre of mass of the object, which is defined as:

$$\boldsymbol{M} = \boldsymbol{Mp} + \boldsymbol{M\tau} \quad (10)$$

where $\boldsymbol{Mp}$ is the fluid pressure moment acting on the body and $\boldsymbol{M\tau}$ is the fluid shear moment acting on the body, which can be obtained by integrating the fluid pressure moment and shear moment acting on the surface of the body, respectively.

2.4. Computational domain conditions and mesh generation

Fig. 1 shows the cylinder and floating ice model. The cylinder was a uniform aluminium solid, which was of 4 slenderness ratio, 50 mm diameter D_0, 200 mm length, 1.06 kg weight. The centre of mass is the centroid of the cylinder. To focus on the investigation of the surface closure case, a typical water entry velocity of 4.2 m/s, was chosen. The floating ice was adopted with a cylindrical shape, with a diameter of D_0 and a thickness of $0.5 D_0$. Owing to the computing resources, the number of floating ice bodies was set to four, which were evenly arranged around the entry point. Initially, the floating ice was in a balanced state of force, and its buoyancy was equal to its own gravity. The water entry point was the intersection point of the diagonal lines of the centre of the four floating ice bodies, and the gap between the cylinder and floating ice was $0.125 D_0$ when the cylinder reached the water entry point.

Vertical water entry (no floating ice) was replaced by "only-water" for ease of differentiation from the ice-water mixture condition. Furthermore, only the cavity shape, the motion, and hydrodynamic characteristics of the cylinder when crossing the ice-water mixture at a low speed are concerned. Additionally, to simplify the computational model and improve calculation feasibility and efficiency, the stress and deformation of the solid were temporarily neglected. During calculation, both the cylinder and the floating ice were regarded as rigid bodies with no relative displacement of the internal particles after being loaded. The direction of the projectile coordinate system was consistent with the ground coordinate system, and the forward direction of the cylinder at the initial time was the same as the x direction of the ground coordinate system and vertically downward. The calculated environmental conditions were divided into two categories: 0 °C only-water condition and 0 °C ice-water mixture condition. The saturated vapour pressure of 0 °C water is 610.47 Pa.

As shown in Fig. 2a, the geometrical dimension of the cuboid computational domain is $26D_0 \times 20D_0 \times 36D_0$, where the water depth is $30 D_0$ and the air domain height is $6 D_0$. The ambient pressure is 101325 Pa. The top section of the computational domain was set as the velocity inlet, and the surrounding and bottom sections were set as the pressure outlet. To enable exchange of data between the floating ice and cylinder during mutual movement through interpolation, the overlapping grid nested in the background fluid domain grid was used to model the surface of the cylinder and floating ice. The underwater pressure changes with the depth of the water and was defined by a custom function $P = \rho_l g h$.

Fig. 2b shows the grid diagram on the xoy section. The mesh adopted the trimmer mesh with better computational performance, and the surroundings and movement of the cylinder area were encrypted to
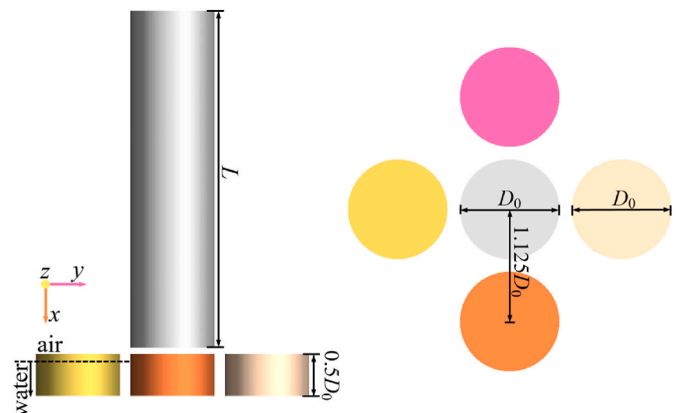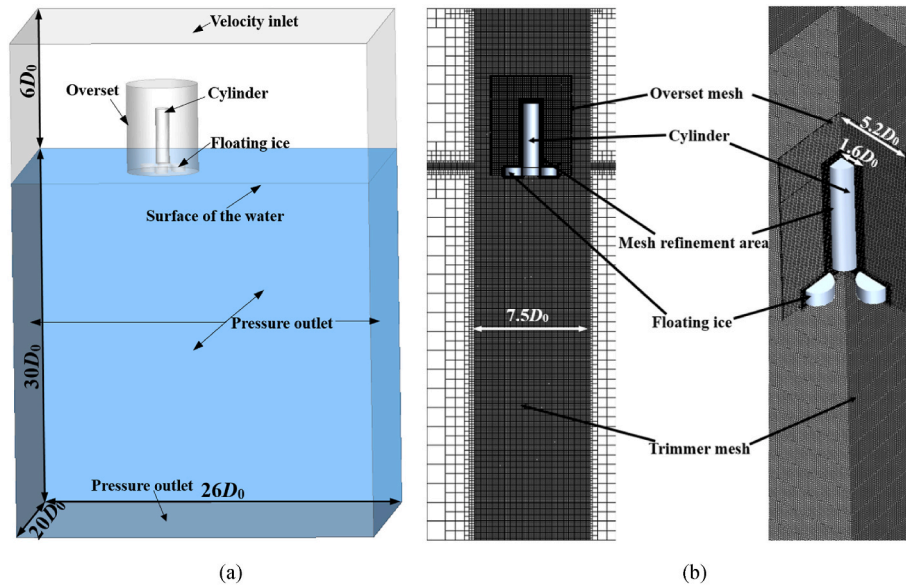

Fig. 1. Cylinder and floating ice model.

Fig. 2. Diagrams of (a) the computational domain and (b) the computational mesh on the *xoy* plane.

obtain more accurate simulation results. The encryption diameter of the moving region is 7.5 D_0, the width of the overlapping grid region is 5.2 D_0, and the refinement region is 1.6 D_0.

To avoid the influence of the mesh density in the boundary layer and the overlapping transition region of the mesh on the calculation results, five different grid cases, i.e., (I)7.63 million, (II)8.81 million, (III)9.72 million, (IV)10.34 million and (V)11.32 million, were selected to verify the mesh independence for the only-water and ice-water mixture conditions. The different minimum mesh densities of the computational domain corresponding to the five grid cases are summarised in Table 1.

Fig. 3 and Fig. 4 show the time histories of the vertical velocity and acceleration curves for the water entry of the cylinder with or without floating ice under different grid cases. After comparison, it can be found that the variation trend and amplitude of velocity and acceleration curves under different grid cases are basically the same, and there is only a slight difference in the cavity necking closure stage with a large numerical fluctuation. Considering ensuring results accuracy and avoiding waste of computing resources, a total mesh size of 9.72 million was selected in the following study.

The value of the non-dimensional wall distance y^+ directly affects the position of the first grid node from the object surface. Because the SST k-ω two equation turbulence model is a high Reynolds number model, y^+ should be less than 1 ($y^+ = (y\rho u_\tau)/\mu$, where y and u_τ are the normal distance and friction velocity of the wall surface, respectively). Hence it is indispensable to verify the maximum value of y^+ on the surface of the cylinder in the water entering process. Fig. 5 shows the calculation results of y^+ distribution on the surface of the cylinder for 9.72 million grids. It can be seen that in the water entry process, the larger area of y^+ was first concentrated on the head of the cylinder when in contact with the water. As the cylinder went deeper, the larger y^+ value began to appear in the tail area and gradually moved downward towards the shoulder. Fig. 6 shows the time history curve of the maximum value of

y^+ on the surface of the cylinder under two conditions. Generally, the amplitude of y^+ changed more sharply in the presence of floating ice, and the y^+ values of the surface of the cylinder under two conditions were all below 1. Furthermore, the amplitude fluctuated greatly in the initial water entry impact and cavity necking closure stages, followed by a downward trend. In conclusion, the corresponding y^+ value at this grid scale can meet the requirements of the SST k-ω two equation turbulence model.

In the present work, the commercial computational fluid dynamics (CFD) software STAR-CCM+ 15.02.007 was used for the simulation. The VOF model was used to simulate the immiscible fluid on the numerical grid, and a VOF wave of still water was established to represent the calm liquid surface. A 6 DOF body was established by combining the overlapping mesh and DFBI model to simulate the cylinder and floating ice, which can be used to calculate the fluid force, torque of the fluid, and the gravity acting on the rigid body, in order to analyse the bidirectional coupling between the liquid and solid phases. The surface tension in the fluid was modelled to obtain a free surface flow, which ensured the stability of fluid dynamics and simulated the water-air interface region more realistically.

The governing equations were discrete by FVM. The time step selected in this study was 1×10^{-4} s to ensure the Courant number was smaller than 1 to achieve stability during calculation. While the time term adopted a one-order implicit scheme, the convection and diffusion terms adopted the second-order upwind and second-order central difference schemes, respectively. The coupling effect of pressure and velocity was solved based on the SIMPLE algorithm (Semi-Implicit Method for Pressure-Linked Equations). Furthermore, the relaxation scheme adopted the Gauss-Seidel method to enhance the convergence of the calculation results.

2.5. Validation of the numerical model

In order to verify the correctness of the established numerical calculation method, an aluminium solid cylinder model, similar to that in the experiment conducted by Hou et al. (2018) was adopted, which is of 200 mm length, 50 mm diameter and 1.06 kg weight. Numerical simulation was carried out according to the initial parameter condition in the literature, which is of 60° water entry angle and 4.35 m/s water entry speed.

Fig. 7 shows the comparison of the cavity shape after water entry obtained from the literature experiment, the literature numerical

Table 1
Mesh densities of the computational domain at five grid cases.

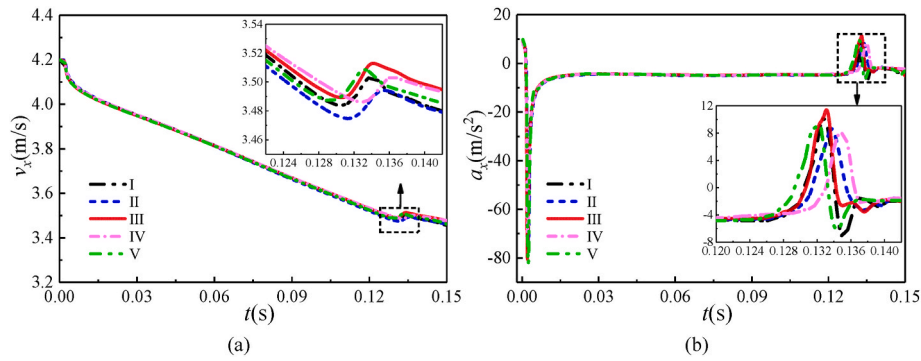| Grid case	Minimum density at overset(mm)	Minimum density at background(mm)	Number of grids (million)
I	3.6	7.20	7.63
II	2.8	5.60	8.81
III	2.0	4.00	9.72
IV	1.2	2.40	10.34
V	0.4	0.80	11.32

Fig. 3. Comparisons of (a) velocity v_x and (b) acceleration a_x in the x direction of the cylinder in the only-water condition under different grid cases.
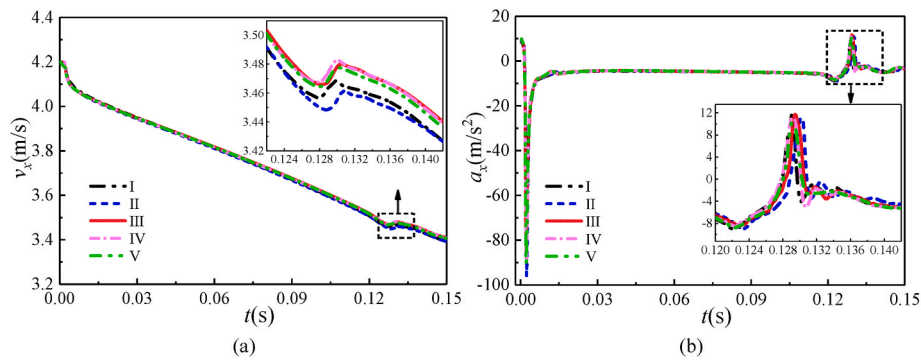

Fig. 4. Comparisons of (a) velocity v_x and (b) acceleration a_x in the x direction of the cylinder in the ice-water mixture condition under different grid cases.
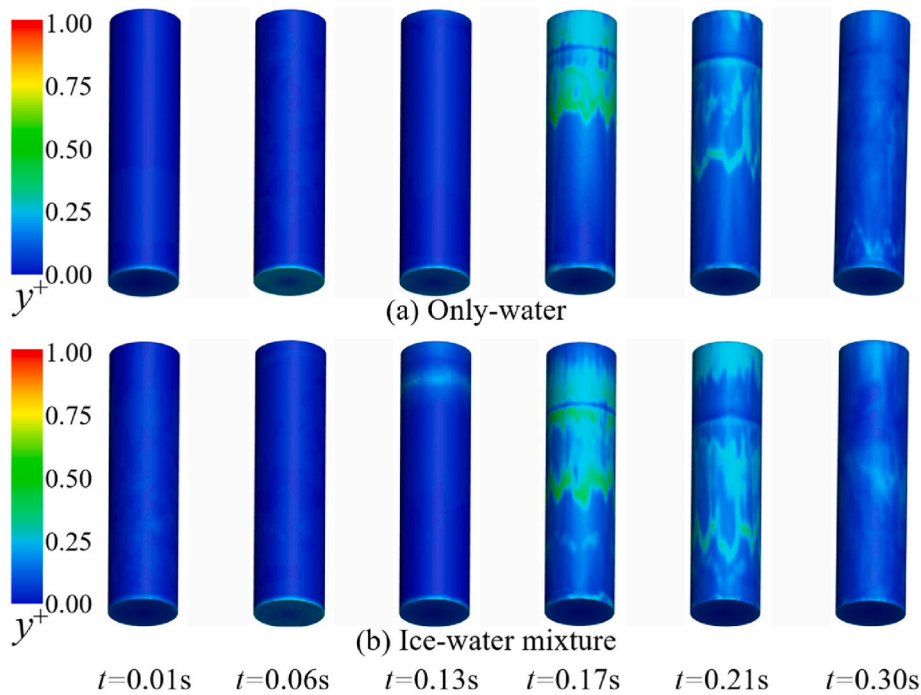

Fig. 5. The distribution of y^+ over the surface of the cylinder under the two conditions. (a) Only-water and (b) ice-water mixture.

simulation and the numerical simulation in this study. Fig. 7a is the water entry cavity diagram recorded by a high-speed camera in the experiment. Under the same condition, the numerical simulation results in the literature are shown in Fig. 7b and Fig. 7c shows the simulation results using the numerical calculation method in this study. The contour of the cavity is described by the isosurface with a volume fraction of

0.5. It can be clearly seen that the development of the cavity can be divided into four stages: the formation of the cavity after impact, gradual reduction of the cavity necking diameter, deep closure, and cavity collapse. Simultaneously, it is verified that the cavity profile obtained from the numerical calculation in this study is consistent with the experimental results in the literature, and the similarity of liquid surface
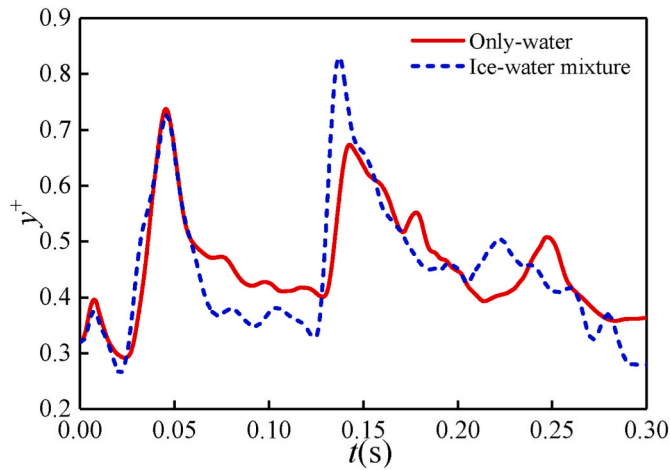
Fig. 6. The time history curve of the maximum value of y^+ on the cylinder surface under the two conditions.

(a) Literature experimental results

(b) Literature simulation results

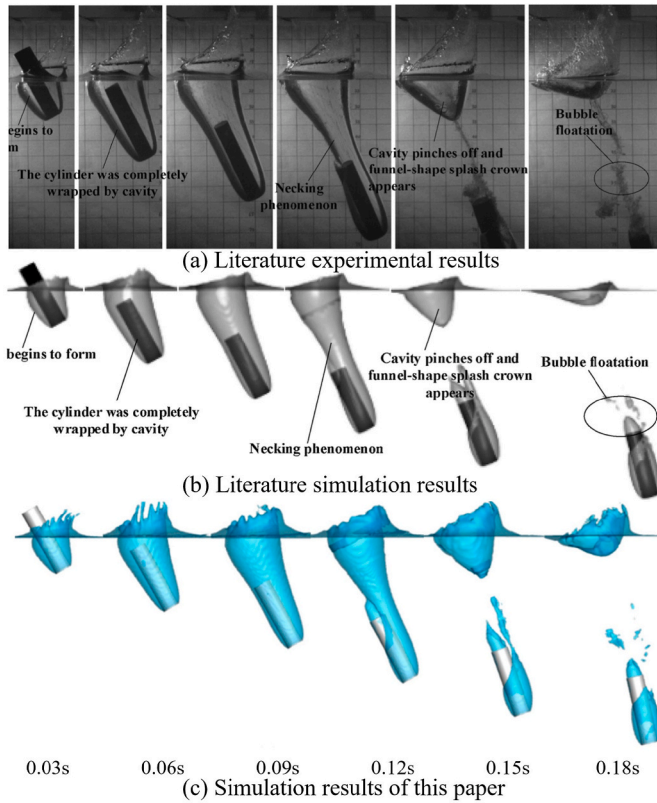(c) Simulation results of this paper

Fig. 7. Comparisons of the cavity shape.

splashing is higher. Furthermore, the numerical calculation method in this study can well capture the flow field changes in the water entering process.

The combined acceleration including horizontal and vertical components of the cylinder is shown in Fig. 8a. The curves of the angle between the cylinder and the initial water surface at different times are shown in Fig. 8b. The transverse and longitudinal axes represent the different times and the cylinder acceleration and angle between the rotation axis of the cylinder and the initial water surface, respectively. The numerical calculation results in this study are observed to be the same as the size and turning trend of the experimental data, and the coincidence degree is high, even closer to the experimental results than the simulation results in the literature. Furthermore, it is verified that

the numerical calculation method used in the study is credible for low-speed water entry problems and is capable of accurately reflecting a series of development processes after water entry.

3. Results and discussion

3.1. Influence of ice-water mixture on the evolution of water entry cavity shape

3.1.1. Evolution process of the water entry cavity

The cylinder passes through the water area with or without floating ice with the same water entry velocity, and the process of the cavity from generation to collapse presents a complex and similar law. The entire process exhibiting significant unsteady characteristics can be divided into four stages: the initial impact stage, open cavity stage, cavity closure stage, and cavity collapse stage. The time when the cylinder reaches the water surface is defined as zero. Figs. 9 and 10 show the unsteady characteristics of the cavity shape evolution of the cylinder entering only-water vertically at a low speed and passing through the ice-water mixture, respectively, where Figs. 9a and 10a are the diagrams of the water volume fraction of *xoy* section and Figs. 9b and 10b are the three-dimensional cavity diagrams. The top view of the cavity evolution under two conditions is shown in Fig. 11.

In the initial water entry impact stage, the cylinder collided with the liquid surface ($t = 0$–0.01 s, Fig. 9). In the only-water condition, the water surface around the cylinder head bulged, causing the liquid to form an annular initial splash. The kinetic energy of the cylinder in motion was transferred to the surrounding fluid particles, resulting in flow separation. The fluid particles expanded in the radial direction perpendicular to the movement of the cylinder to form a cavity. However, when the cylinder collided with the water surface through the floating ice gap (Fig. 10), not only does its own kinetic energy need to be converted into the kinetic energy of water to promote expansion of the liquid to form a cavity, but also into the movement of the floating ice. Considering the initial velocity into the water was the same, the kinetic energy used by the cylinder for transformation was fixed. Therefore, under the influence of floating ice, the kinetic energy obtained by the liquid was significantly reduced, thereby weakening its expansion speed and the formation speed of the cavity. Finally, the volume of the initial cavity was significantly smaller than that of the only-water condition, which indicates that floating ice has a hindering effect on the diffusion of liquid. The floating ice is solid, and its inertia and influence by gravity are much larger than those of the fluid. Moreover, the floating ice also hindered the development of the splash, resulting in a large difference in the shape of the initial splash. Owing to the hindrance of the floating ice, the liquid with certain kinetic energy could only spatter out from the gap between the floating ice, resulting in the failure to form an annular water curtain that was uniformly higher than the water surface. However, it showed a "slender arrow-shaped" splash with a smaller volume and faster speed ($t = 0.03$ s, Fig. 10b). Owing to the influence of floating ice, the open cavity stage and cavity closure stage of the two conditions were no longer the same, which will be discussed separately.

In the open cavity stage ($t = 0.01$–0.06 s) under the only-water condition, the cylinder continued to go deeper, and the external air continued to influx from the outside due to the pressure difference inside and outside the cavity, which resulted in further expansion of the cavity to form an open cavity ($t = 0.03$ s). The cavity elongated continuously while expanding radially. 0.06 s after entering the water, the cylinder was completely wrapped by the cavity. During the cavity closure stage, the splash phenomenon on the free liquid surface became more obvious as the cylinder deepened, causing the thickness of the annular water curtain to increase. Furthermore, the liquid was affected by complex factors such as surface tension, gravity and aerodynamic force near the cavity mouth, causing the kinetic energy of fluid particles in the outward spatter to decrease. The annular water curtain shrank and fell back to the central axis, and gathered over the water surface to form a closed bell jar
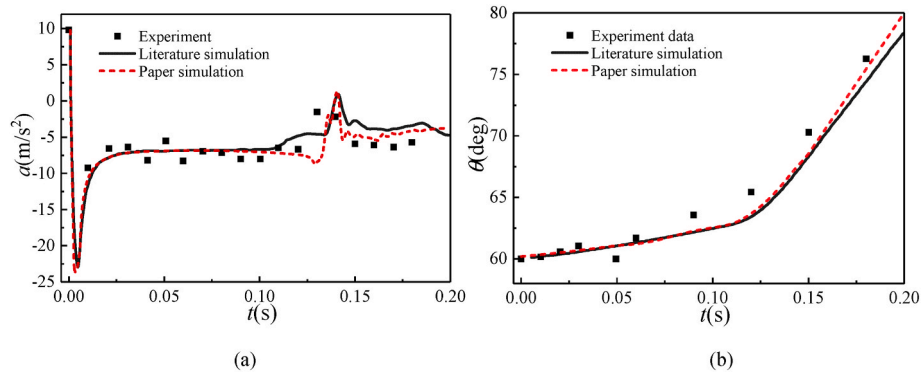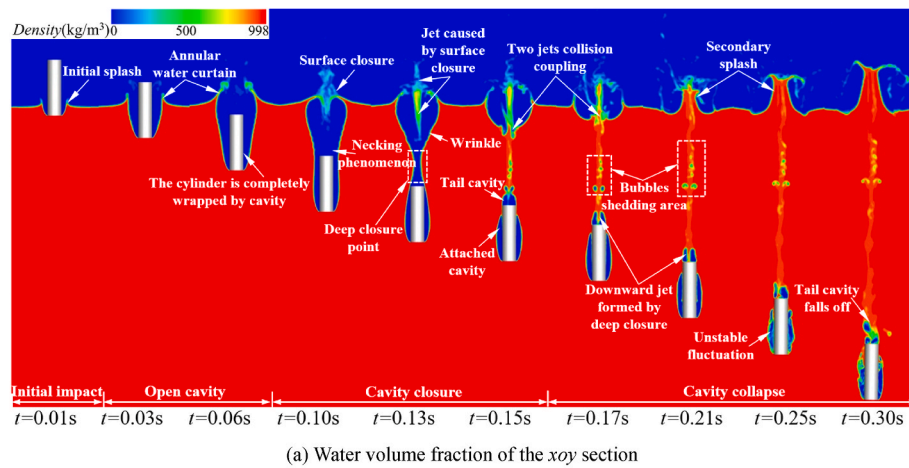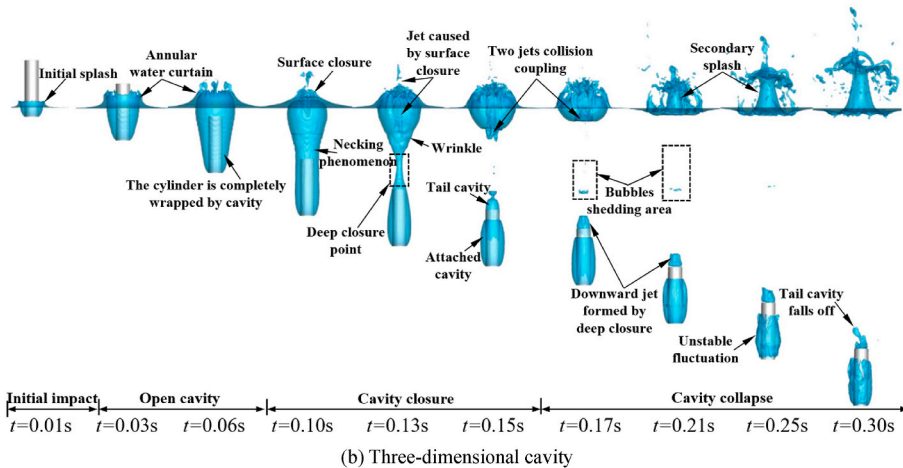
Fig. 8. Comparisons of (a) acceleration *a*, (b) angle displacement *θ* between the experiment and numerical simulation.

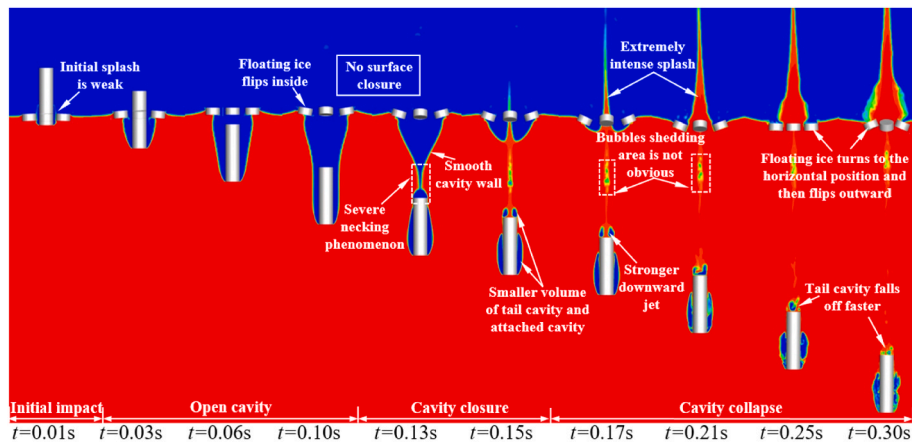(a) Water volume fraction of the *xoy* section

(b) Three-dimensional cavity

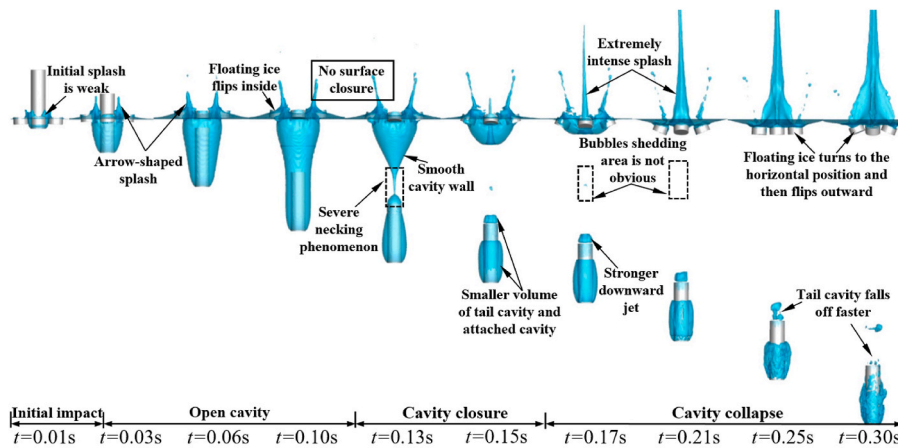**Fig. 9.** Cavity shape evolution in the only-water condition.

to separate the cavity from external air, resulting in a surface closure (*t* = 0.10 s). Simultaneously, the water curtain gathered at the impact point to form two upward and downward jets. The downward jet was stronger than the upward jet owing to the fact that the direction of the combined movement of the fluid particles was downward during the impact.

As the water entry depth of the cylinder increased, the pressure difference inside and outside the cavity increased, and the speed of the radial expansion of the cavity gradually decreased to zero. As a result, the cavity began to accelerate inward contraction, resulting in a necking phenomenon. The evolution process of the cavity shape at the characteristic time of 0.10–0.15 s is shown in Fig. 12a. As time passed, more and more fluid particles participated in the falling movement, which

further enhanced the downward retroreflection flow, whereas the thickness of the bell jar cover film became thinner. Under the compound effect of the retroreflection flow impingement and gas leakage during necking, the closed bell-shaped cover collapsed and broke near the impact point 0.12 s after entering the water, and the cavity once again connected to the outside world. At 0.13 s, the cavity near the tail of the cylinder was close to the surface of the cylinder because of the cavity necking, and the cavity was about to deeply close. At this time, the downward jet generated by the surface closure exhibited a low velocity and was far from the cylinder, hence it did not catch up with the cylinder. However, the cavity above the deep closure point was significantly affected by the disturbance of the downward jet droplets, and the
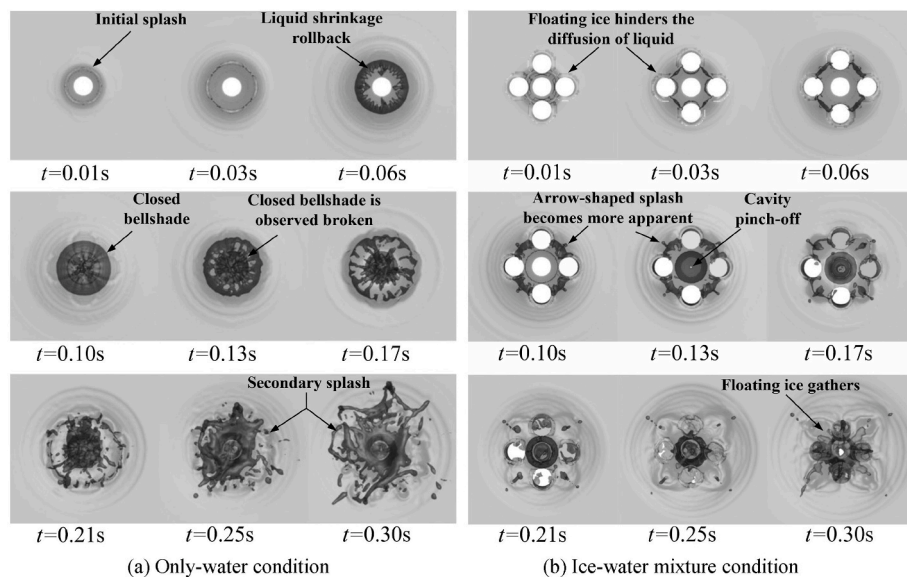
(a) Water volume fraction of the *xoy* section

(b) Three-dimensional cavity

Fig. 10. Cavity shape evolution in the ice-water mixture condition.

(a) Only-water condition

(b) Ice-water mixture condition

Fig. 11. Top view of cavity evolution.

cavity wall was disordered and generated obvious wrinkles. Subsequently, the cavity shrank to a point in a very short time to form a deep closure, and the cavity divided into two cavities with different volumes.

Owing to the deep closure of the cavity, the cavity wall collided in the horizontal direction to form two high-speed jets in directions to the free liquid surface and the motion direction of the cylinder, respectively. The
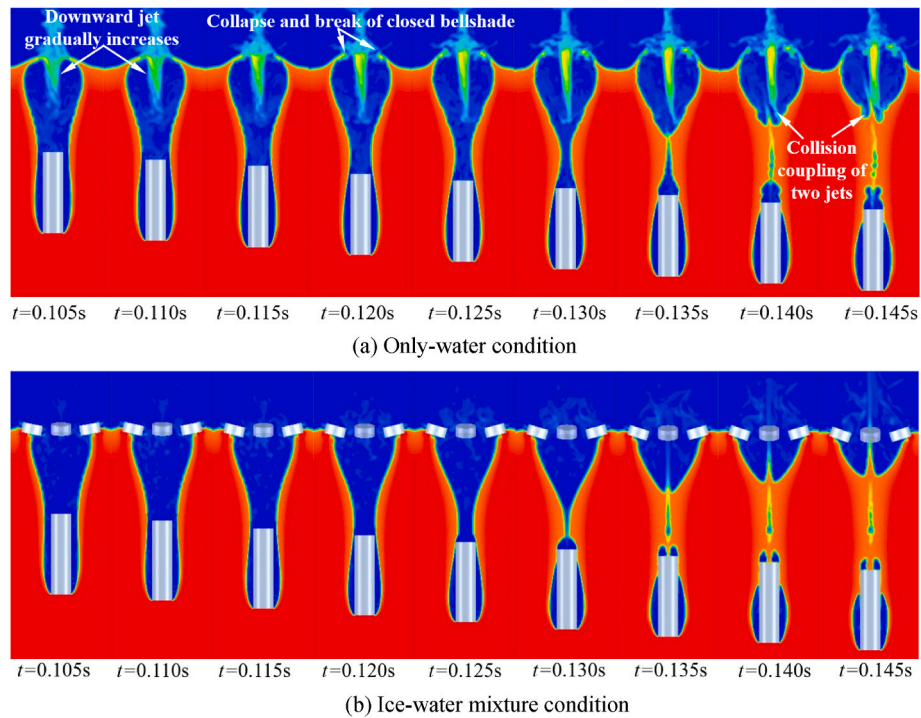
Fig. 12. Evolution process of the cavity shape at characteristic time of 0.10–0.15 s.

upward jet collided with the previous jet at 0.14 s, making the flow field near the free liquid surface more complicated. This phenomenon will be further analysed in the cavity collapse stage.

Under the condition of ice-water mixture, the open cavity stage (t = 0.01–0.10 s) was affected by the floating ice, the expansion speed of the cavity was slower, and the opening duration of the cavity was longer than that of the only-water condition. After the cylinder hit the water, it continued to go deep, the floating ice diffused outward, and the diameter of the cavity mouth increased gradually. Although the shapes of the cavity under the two conditions below the free surface were almost the same during this period, the difference in the phenomenon near the free surface became obvious. In the ice-water mixture condition, the slender arrow-shaped splash was fast and extremely high in a very short time (Fig. 10b), and the surface closure did not form for 0.10 s after entering the water. Furthermore, the diameter of the cavity mouth and cavity volume were larger than those of the only-water condition.

When the cylinder reached a certain depth under water, the kinetic energy of the liquid spreading outwards near the cavity mouth began to decay, and the liquid began to shrink and roll back inward. The existence of floating ice hindered the contraction and rollback of the liquid, and the outer edge of the floating ice flipped inward owing to the force of the fluid's inward contraction (t = 0.10 s). The cylinder continued to deepen in water, and the cavity wall shrank owing to the pressure difference inside and outside the cavity, thereby entering the stage of cavity closure (t = 0.10–0.15 s, Fig. 12b). Although the tail cavity of the ice-water mixture in the cavity closure stage was still connected to the external atmospheric environment, the necking phenomenon in the cavity was more severe than that of the only-water condition, and a large amount of air in the cavity was squeezed and moved quickly to the liquid level. On comparing Fig. 12a and b, it can be seen that while the cavity shape below the free surface was almost the same before 0.12 s in both conditions, the existence of floating ice significantly influenced the development of the cavity after 0.12 s. At 0.13 s, the cavity in the necking section had not yet closed in the only-water condition, and that around the cylinder tail only contacted the bottom edge of the cylinder. However, the cavity in the necking section had closed at a point above the cylinder at the same time in the ice-water mixture condition. The

cavity was separated into two parts, one was a funnel-shaped cavity near the free surface moving upwards, and the other, attached to the surface of the cylinder, was moving downward. Considering the cavity in the ice-water mixture condition did not form a surface closure, no jet disturbance occurred, and the cavity wall above the deep closure point was relatively smooth without wrinkles.

In both cases, the cavity entered the collapse stage after 0.15 s. In the only-water condition, the deep closure caused the cavity around the cylinder to close on the surface of the cylinder, thereby forming a closed tail cavity and a relatively stable semi-enclosed attached cavity. The liquid at the deep closure point accumulated and collided, resulting in two upward and downward jets, and a large number of bubbles formed after the cavity were squeezed and broken. The upward jet moved at a high speed towards the free liquid surface and collided with the downward jet generated by the previous surface closure. Considering the upward jet was more intense, the two jets were coupled to form an upward spray jet, which caused the secondary splash. As shown in Fig. 11a, the secondary splash was distorted and irregular owing to the effect of the collision of the two jets in the upper and lower directions. After 0.13 s, the upward splashing jet became more obvious due to the large number of fluid particles participating in the movement. Considering the velocity of the downward jet was much larger than the downward velocity of the cylinder, it rapidly caught up with the cylinder and continued to impact its tail surface, thereby impacting the motion trajectory of the cylinder, resulting in gradual deflections. Furthermore, bubbles shedding occurred after the deep closure of the cavity (t = 0.17 s). Affected by buoyancy and external water pressure, the bubbles rose along the cylinder's water entry trajectory and formed a bubbles shedding area. The width of the area was approximately the same as the diameter of the cylinder. At approximately 0.25 s, the instability fluctuation gradually appeared near the cavity wall around the cylinder, and the attached cavity and tail cavity fell off asymmetrically, which further led to the deflection of the cylinder.

The cavity collapse stage (t = 0.15–0.30 s) in the ice-water mixture was quite different from that in the only-water condition owing to the influence of the floating ice. Because the necking phenomenon was more intense, the degree of liquid collision at the deep closure point was more

severe, resulting in greater intensity of the two upward and downward jets. However, no downward jet occurred near the cavity mouth of the free liquid surface, hence the strong jet generated by the deep closure exhibited an unimpeded upward movement with extremely high splashing. As more fluid particles participated in the movement over time, the intensity of the secondary splash was further aggravated. As shown in Figs. 10b and 11b, the secondary splash exhibited a regular shape, like an arrow. Compared with the only-water condition, the stronger necking caused the cavity to be close to the bottom of the cylinder surface, resulting in a smaller volume of tail cavity and attached cavity ($t = 0.17$ s), higher wetted degree of the cylinder, and far less obvious bubbles shedding area. Furthermore, the width of the area was narrow, only one third of the diameter of the cylinder. On comparing Figs. 9 and 10, it could be clearly observed that while the tail cavity gradually fell off in the cavity collapse stage in the only-water condition, the volume change is not obvious. However, the tail cavity of the ice-water mixture condition fell off faster and shed completely at 0.30 s. At this stage, the floating ice was greatly deflected by the fluid force at the free surface. At 0.15 s, the floating ice reached the edge of the funnel-shaped tail cavity and turned inward by the inward contraction force of the fluid. The jet generated by the deep closure quickly splashed upward, causing the floating ice first to flip inside and then rotate outside. At 0.25 s, the floating ice turned to the horizontal position and continued to be affected by the upward secondary splash impact, gradually flipping outside ($t = 0.30$ s).

3.1.2. Variation law of the cavity diameter in different water depths

In order to quantitatively analyse the variation law of the cavity diameter with time at different water depths from the unperturbed liquid surface, the curves of the cavity diameter with time at water depths of D_0、2.5 D_0、4.5 D_0 (cavity deep closure position) and 6 D_0 in the time range of 0.02–0.15 s after entering the water are shown in

Fig. 13. The data of each condition was obtained by taking the average of multiple measurements based on the cavity contour diagrams calculated at different times, and the curves were obtained after polynomial fitting. The transverse axis is the water entry time of the cylinder, and the longitudinal axis was treated with dimensionless processing using the following equation:

$$\overline{D} = \frac{D_c}{D_0} \tag{11}$$

where D_c is the diameter of the cavity at the specified section, D_0 is the diameter of the cylinder, and X is the vertical distance from the specified section to the undisturbed free surface.

As shown in Fig. 13, the cavity diameter at different water depths in both conditions shows obvious nonlinear changes. The curves on different sections experienced the expansion and contraction stages. As the water depth where the cavity was intercepted increased, the maximum diameter of the cavity gradually decreased. Furthermore, the duration of the expansion stage was reduced significantly, and the variation range of the cavity diameter was expanded significantly. Although the variation law of cavity diameter under the conditions with or without floating ice was similar to a certain extent, the cavity diameter differed with time. According to the principle of independence of the cavity section expansion, the subsequent development of the cavity section at any water depth is only related to the conditions at the initial moment of the section. Moreover, there is little interaction between the cavities at different water depths, and the degree of cavity expansion is only determined by the flow state of the liquid when the cylinder reaches this position. According to the velocity curve (Fig. 24b), the velocity in the vertical direction of the cylinder in the two conditions was the same before 0.11 s. However, as shown in Fig. 13, the change in the cavity diameter in the two conditions was quite different. Therefore, we can conclude that the existence of floating ice significantly
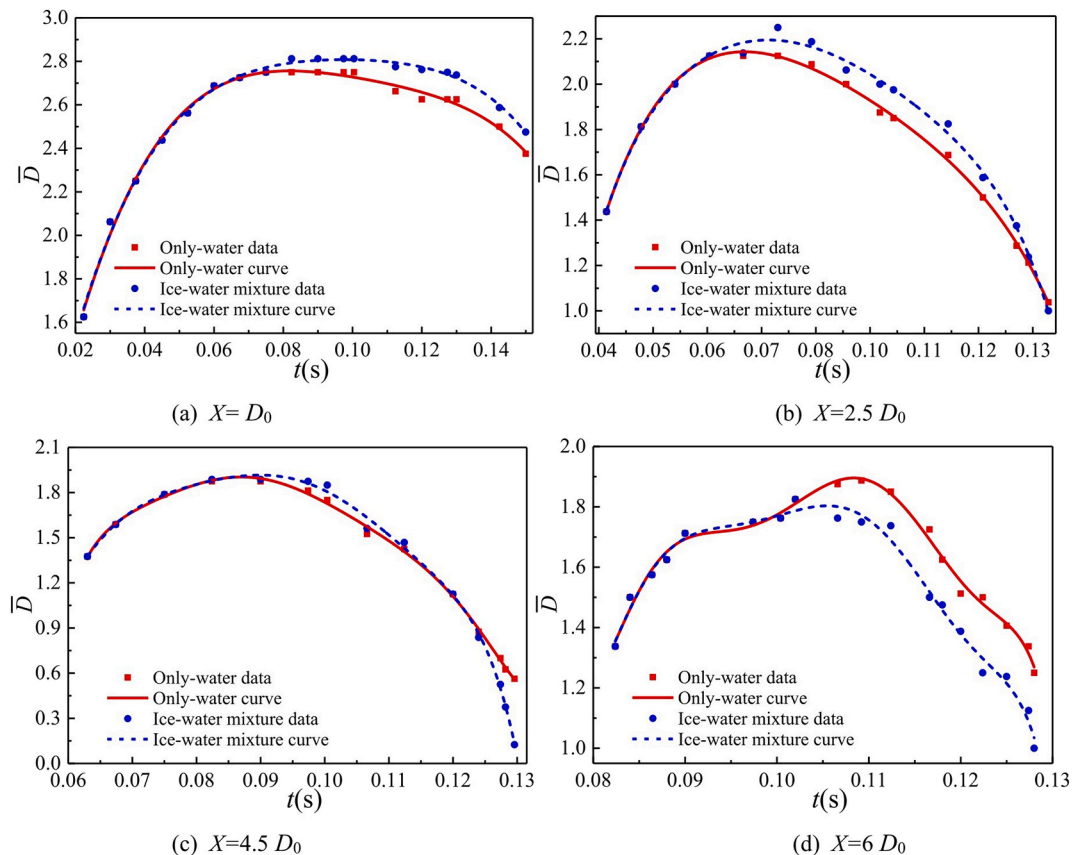

Fig. 13. Variation law of cavity diameter ($\overline{D}$) at different water depths (X).

influenced the change in the cavity diameter at different water depths.

Fig. 13a shows the variation of the cavity diameter close to the free liquid surface. The cavity diameter of the two conditions began to differ after 0.07 s of the cylinder entering the water, considering the surface closure phenomenon only occurred in the only-water condition during this period. Owing to the water depth of the selected section is close to the free liquid surface, the cavity diameter in the only-water condition gradually reduced due to the shrinkage and aggregation of the liquid during surface closure. However, surface closure did not occur in the ice-water mixture condition, hence, the cavity of this section lasted for a long time at the maximum diameter, and then the cavity necking occurred. The cavity diameter of ice-water mixture condition began to decrease. However, considering the position of the selected section is far from the necking position, the change of cavity diameter in the two conditions is not obvious.

Fig. 13b shows the variation in the cavity diameter in the middle section between the undisturbed liquid surface and the deep closure point. Because the cavity diameter at this section in the only-water condition was still affected by the surface closure, it contracted earlier than that in the ice-water mixture. Additionally, owing to its proximity to the necking position, the diameters of the two conditions changed significantly. The change rates of cavity diameter in the two conditions were almost the same before 0.115 s. Because the deep closure of the ice-water mixture condition appeared earlier, the diameter of the cavity at this section decreased rapidly due to the contraction and accumulation of liquid, and the diameter of the cavity was consistent with that of the only-water condition at 0.13 s.

As shown in Fig. 13c, because the deep closure position of the cavity is far from the free surface, the surface closure phenomenon had little effect on the cavity diameter of the section at this position, and only a small difference was observed between 0.09 and 0.11 s after entering the water. After 0.125 s, the necking phenomenon intensified, and deep closure was about to occur. Owing to early deep closure in the condition of ice-water mixture, the reduction rate of cavity diameter increased rapidly and decreased to 0 first.

The cavity section in Fig. 13d is located below the deep closure point, where the cavity was around the cylinder. Owing to the influence of cavity necking and deep closure, the nonlinearity of the cavity diameter change was stronger. A difference was observed in the cavity diameter before and after 0.11 s. As shown in Fig. 12, the volume of the cavity around the cylinder in the ice-water mixture condition was slightly smaller than that of the only-water condition, and the cavity around the cylinder was closed on the surface of the cylinder with the variation trend of the cavity diameter being the same in both conditions.

3.2. Influence of ice-water mixture on the characteristics of flow fields

During the process of the cylinder entering the water, the flow field structure became extremely complex due to the unsteady cavity evolution, and the existence of floating ice further affected the change of the flow field structure. In order to further analyse the similarities and differences in the flow field structure characteristics during the process of the cylinder vertically entering only-water at a low speed and passing through the ice-water mixture, the velocity field distribution, pressure field distribution and unsteady vortex structure characteristics under both conditions were deeply compared and analysed.

3.2.1. Velocity field distribution characteristics

Figs. 14 and 15 show the top view of the velocity field distributions on the free liquid surface and *xoy* section in the two conditions, respectively. The velocity contour and velocity vector line are combined to study the velocity field distribution, wherein the red and blue parts indicate the high-velocity and low-velocity areas, respectively, and the arrowhead direction indicates the moving direction of the fluid particles.

In the initial water entry impact stage, the velocity field symmetry of the two conditions was excellent. In the only-water condition, the surrounding gas was driven by the water entry process of the cylinder, and a high-velocity gradient appeared at the tail of the cylinder. Owing to the influence of the initial splash and initial cavity, the external air rapidly poured into the cavity, and an obvious high-velocity gas flow area appeared near the head and shoulder of the cylinder. The gas flow
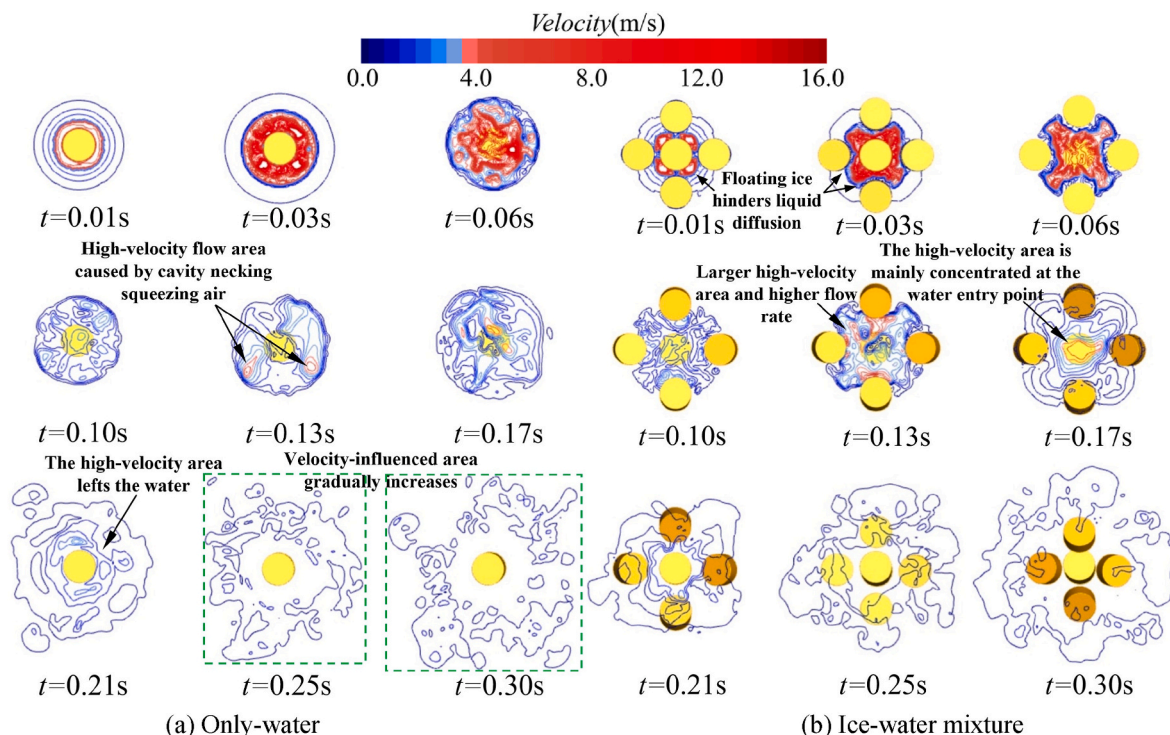

Fig. 14. Top view of velocity field distribution on free liquid surface.
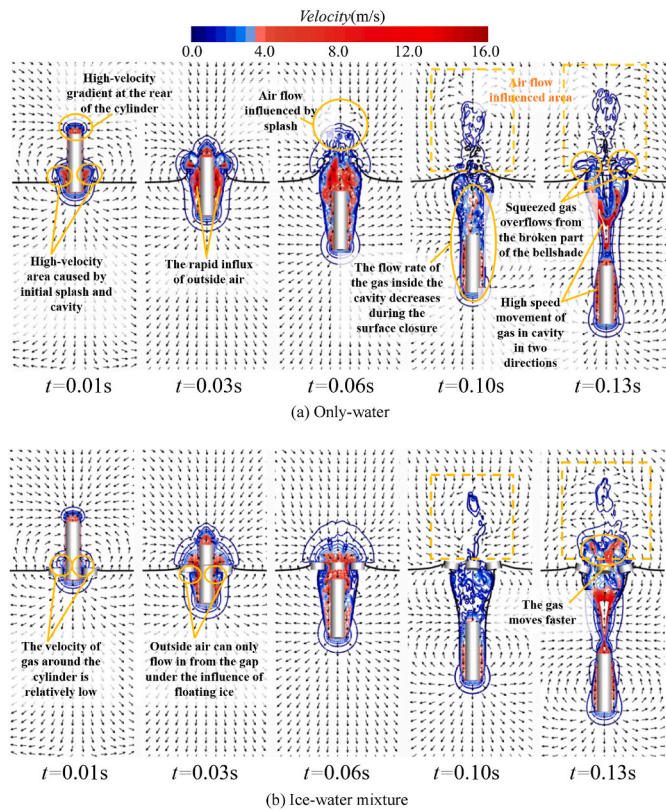
Fig. 15. Velocity field distribution on the *xoy* section before 0.15 s.

velocity reached 3 to 4 times the cylinder's entry velocity. In the condition of ice-water mixture, the roundness of the velocity contour in the top view decreased owing to the floating ice because it hindered the liquid diffusion process (Fig. 14b). On comparing Fig. 15a and Fig. 15b, it can be found that under the influence of floating ice, the gas could only enter the initial cavity from the tiny gap between the cylinder and floating ice, resulting in an unobvious high-velocity flow area of the air at the head and shoulder of the cylinder.

In the open cavity stage, the fluid motion characteristics of the two conditions were more obvious than those in the initial water impact stage, and a large amount of external air flowed into the cavity to promote the development of the cavity. As shown in Figs. 14a and 15a, the high-velocity area in the only-water condition expanded significantly in a short time (*t* = 0.01–0.06 s). The initial splash transmitted the kinetic energy outward, and the air above the free surface flowed under the influence of liquid splash. Between 0.06 and 0.13 s, the velocity of gas flow inside the cavity was relatively slow, which indicated that the cavity had entered a stable development stage before surface closure. The jet generated by surface closure further expanded the affected area of air flow above the free liquid surface, resulting in a flow of far-field air. Owing to cavity necking, the gas in the cavity at the deep closure point was divided into two parts: one large and one small (*t* = 0.13 s). The direction of the velocity vector arrow inside the cavity indicates that the gas above the closure point exhibited a larger volume and moved at a high speed to the free liquid surface under liquid pressure. After breaking the closed bell jar, it was discharged from the gap. The gas below the closure point remained in the cavity and moved downward at a high flow rate.

At the same stage, the phenomenon of ice-water mixture condition was significantly different from that of only-water condition. As shown in Figs. 14b and 15b, at 0.03 s, the influx of external air was still obviously hindered by the floating ice. The outside gas could only flow in rapidly from the gap between the floating ice and cylinder, hence the high velocity flow area below the floating ice was narrow. Although no

surface closure was observed at 0.10 s, the velocity vector line at that time indicated that the far-field air above the free surface was still affected by the gas leakage during necking. At 0.13 s, the gas above the closed point was squeezed more strongly by the external fluid of the cavity and reached a very high moving speed. Even a high-velocity area above the free liquid surface was generated, which was not observed in the only-water condition. Fig. 14 shows the difference in flow velocity at the free surface between the two conditions at 0.13 s. Although the area of high velocity generated at the free surface of only-water condition was small, the area of high velocity at the free surface of ice-water mixture condition was larger, and hence exhibited higher speed.

Considering the density of air is two orders of magnitude lower than that of water, the necking phenomenon significantly impacted the gas flow velocity. In order to quantitatively and intuitively analyse the difference in gas velocity caused by deep closure, the variation of the maximum velocity of high-speed moving gas generated by deep closure with time in the two conditions after 0.13 s was evaluated, as shown in Fig. 16. It can be seen that the maximum peak value of the gas flow velocity in the two conditions was extremely high (77.09 m/s and 122.13 m/s), reaching 18.4 and 29.1 times the water entry velocity of the cylinder, respectively. And the time and size of the peak value are obviously different.

The reason for this difference is shown in Fig. 17. The curve in the figure represents the flow pressure variations (relative atmospheric pressure) along the radial axis at the deep closure point ($X = 4.5\,D_0$), and the hollow circle on the curve represents the junction point between the cavity wall and the liquid at the depth of the water. At 0.126 s, the pressure difference inside and outside the cavity in the ice-water mixture condition was larger than that of only-water (Fig. 17a), resulting in a stronger necking phenomenon in the ice-water mixture condition. The liquid shrinkage caused a slight increase in the pressure inside and outside the cavity in the two conditions, and the increase in the ice-water mixture condition was larger (Fig. 17b). The cavity diameter at the deep closure in the two conditions both became smaller.

At 0.130 s, the deep closure began to appear in the ice-water mixture condition, and the cavity shrank rapidly. The pressure at the centre of the deep closure was extremely high, reaching 35000 Pa. The gas above the closure point was driven by high pressure to the low-pressure area near the water surface, and thus was accelerated to a very high speed. At this time, the only-water condition was still in the necking stage. The pressure difference inside and outside the cavity was relatively small, and the gas had not yet obtained a large acceleration (Fig. 17c). After that, only-water condition appeared deep closure (*t* = 0.132 s, Fig. 17d). A high pressure peak appeared at the deep closure point, but the pressure peak was lower than that of the deep closure point of ice-water
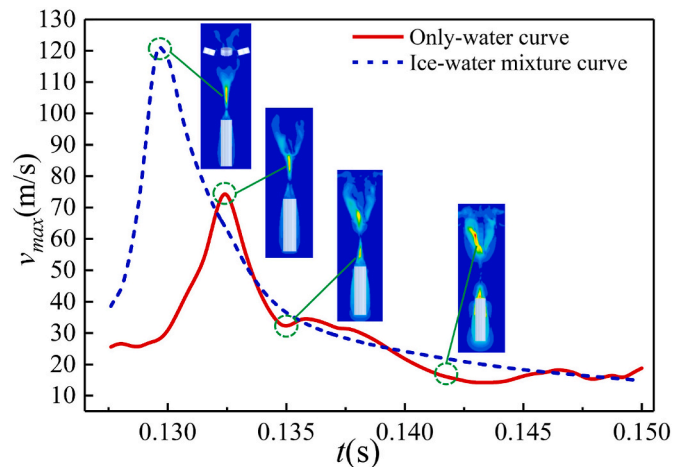

Fig. 16. Time histories of the maximum gas velocity v_{max} in cavity before and after deep closure.
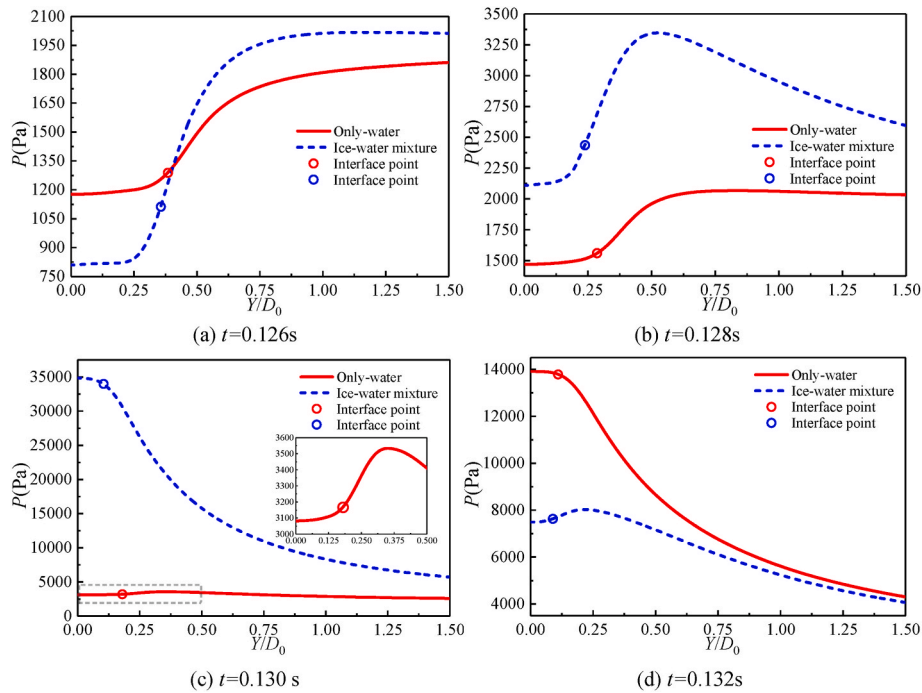
Fig. 17. The flow pressure variations along the radial axis at deep closure point ($X = 4.5\ D_0$).

mixture condition, only 14000 Pa. And the acceleration obtained by gas was smaller, so the maximum velocity peak of the two conditions was different. At this time, the pressure at the deep closure point in the ice-water mixture condition decreased rapidly, indicating that the pressure increase at this point was not persistent and belonged to the transient phenomenon.

It can also be found from Fig. 16, the variation of gas velocity under different conditions was obviously different. The maximum gas velocity curve in the ice-water mixture condition increased rapidly owing to the intense necking in the early stage, whereas the change was relatively gentle in the later stage. However, in the only-water condition, the maximum velocity curve of gas flow increased gradually in the early stage due to a small necking degree, but it fluctuated significantly in the later stage. The inflection points and specific position of the maximum gas flow rate varied with time were different for both conditions. Due to the unimpeded upward overflow of gas in the condition of ice-water mixture, the position of the maximum gas velocity point in the ice-water mixture condition all appeared above the deep closure point, but the spatial position of the maximum gas velocity point in the only-water condition changed several times, as follows: The velocity of the upward high-speed moving gas near 0.135 s decreased sharply owing to the obstruction of the downward jet generated by the surface closure. At this time, the maximum downward moving gas velocity caused by the necking extrusion was greater. At 0.142 s, the kinetic energy of the downward moving gas decayed when it impacted the tail of the cylinder. Additionally, the upward moving gas velocity was greater.

In the cavity collapse stage (t = 0.15–0.30 s), the downward and upward jets formed by the surface closure and deep closure of the cavity, respectively, collided and coupled in the only-water condition at 0.15 s, as shown in Figs. 14a and 18a. The shape of the secondary splash was distorted, and its direction was tilted, which was not entirely on the axis of the cylinder. Furthermore, the gas velocity inside the tail cavity and attached cavity was relatively high. As the depth of the cylinder entry increased, the velocity of the internal gas in cavity gradually decreased, and the cavity began to collapse. Owing to the participation of a large number of fluid particles, secondary splash gradually developed upward, and its influence on far-field air flow expanded further.

The phenomenon of liquid surface splash and internal flow velocity

of the cavity in the collapse stage in the ice-water condition was different from that of the only-water condition. At 0.17 s, the jet at higher speed splashed extremely high, and the area of high velocity was much larger than that of the only-water condition. As shown in Fig. 18b, the high-velocity area around the free liquid surface in the ice-water mixture condition at this time was almost all concentrated on the axis of the cylinder. Between 0.25 and 0.30 s, the attenuation rate of gas velocity in the tail cavity and attached cavity was greater, and the high-velocity area in the cavity almost disappeared at 0.30 s.

3.2.2. Pressure field distribution characteristics

Fig. 19 shows the pressure (relative atmospheric pressure) distribution at typical moments during the process of the cylinder vertically entering only-water at a low speed and passing through the ice-water mixture, which was used to investigate the spatial distribution characteristics of the pressure field and its variation law with time.

In the initial water impact stage (t = 0–0.01 s) of the only-water condition, owing to the influence of the severe impact on the water surface, a high-pressure area appeared in front of the cylinder head and propagated in a spherical form in the circumferential direction. The closer it was to the cylinder head, the greater the pressure and its gradient were. The cylinder carried a large amount of air while entering the water. According to the Bernoulli principle, owing to the high velocity of airflow around the head, a low-pressure area appeared. The external air flowed into the cavity due to the pressure difference inside and outside the cavity, which further increased the cavity volume and formed an open cavity. As time passed, at 0.06 s, the shape of the low-pressure area around the cylinder was consistent with the shape of the cavity, and the cavity entered a stable expansion period (t = 0.06–0.10 s), and the internal pressure of the cavity gradually stabilised to the same as the external atmospheric pressure. The pressure distribution characteristics of the ice-water mixture condition before 0.10 s were roughly the same as those in the only-water condition, which will not be described again.

Between 0.10 and 0.13 s, although the cavity necking phenomenon occurred in both conditions, the pressure distribution of the flow field was quite different. At 0.10 s, the surface closure of the cavity near the free liquid surface occurred in the only-water condition, and the cavity
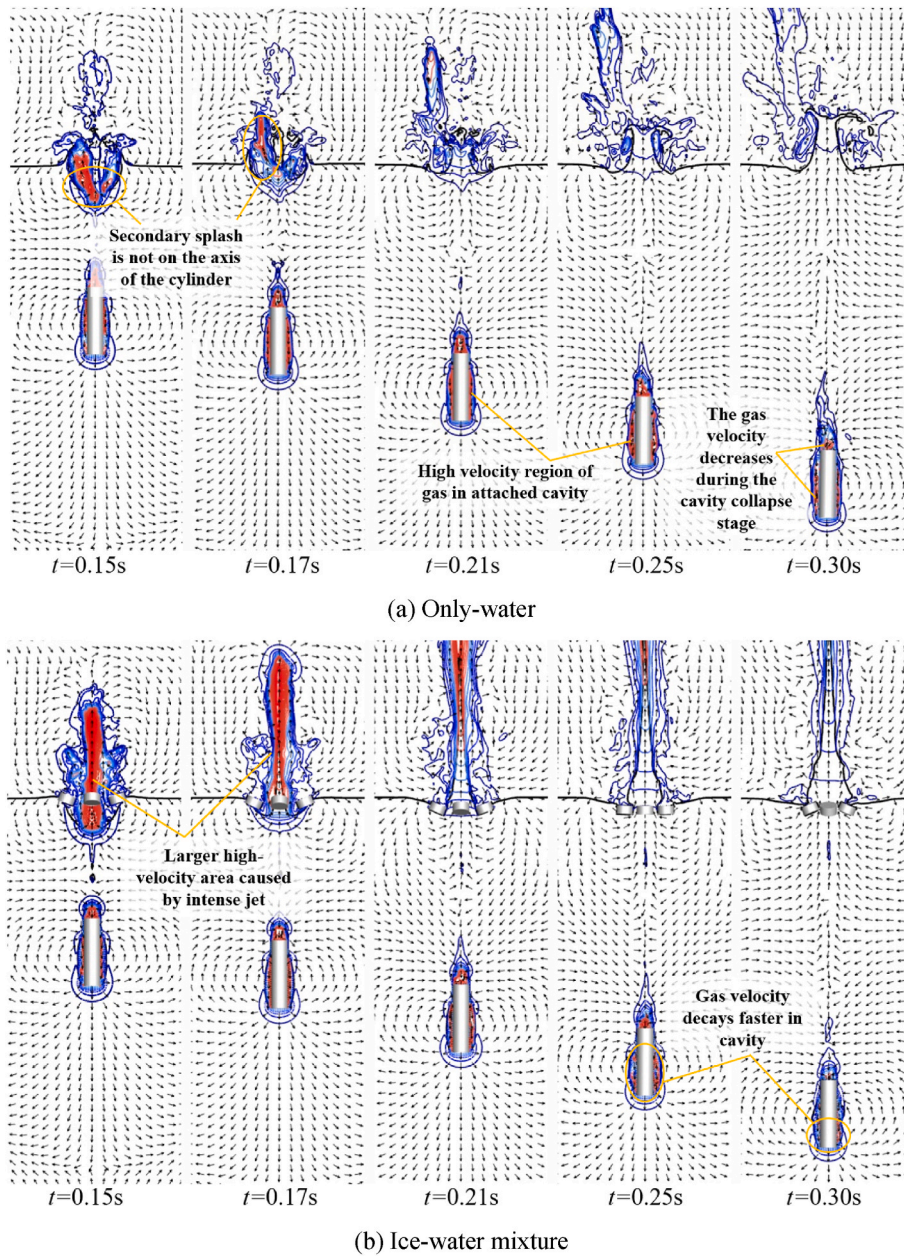
Fig. 18. Velocity field distribution on the *xoy* section after 0.15 s.

separated from the external environment. Due to the influence of the surrounding fluid particles on complex factors such as cavity extrusion and jet impact, the overall internal pressure of the cavity increased slightly and became larger than the external atmospheric pressure. As time passed, the internal pressure of the cavity gradually increased (*t* = 0.11 s) until the closed bell jar collapsed and broke.

At 0.12 s, the cavity pressure near the free surface was reduced to atmospheric pressure. However, the internal pressure of the cavity near the necking section was still high. The necking was then intensified (*t* = 0.13 s) and the cavity shrank continuously. A high-pressure area appeared from the deep closure point to the tail of the cylinder. Because the gas in the cavity was compressed to form upward and downward jetting airflow, the downward high-speed airflow impacted the tail of the cylinder, which resulted in a sudden increase in the force and pressure gradient at the head of the cylinder. Owing to the impact of the upward jet, the collapse degree of the closed bell jar intensified, and the cavity connected to the outside again. At this time, the internal pressure of the cavity, except for the necking section, decreased and became

equal to the atmospheric pressure.

The ice-water mixture condition was affected by the floating ice, and the surface closure was not formed during the whole water entry process. The cavity had always been connected to the external environment, and the internal pressure was maintained near atmospheric pressure. Therefore, between 0.10 and 0.12 s, the pressure difference inside and outside the cavity grew larger than that of the only-water condition, which can also be seen from Fig. 17, thereby causing a more severe necking phenomenon compared to that of the only-water condition, which made the deep closure appear earlier. On comparing Fig. 19a and b, it could be seen that the liquid at the deep closure point in the ice-water mixture condition collided at 0.13 s and formed a very high-pressure area at the impact point. At the same time, the pressure at the wet end of the cylinder was high, which significantly influenced the motion characteristics of the cylinder. Moreover, the high-speed movement of a large amount of gas formed by extrusion resulted in an obvious low-pressure area above the deep closure point.

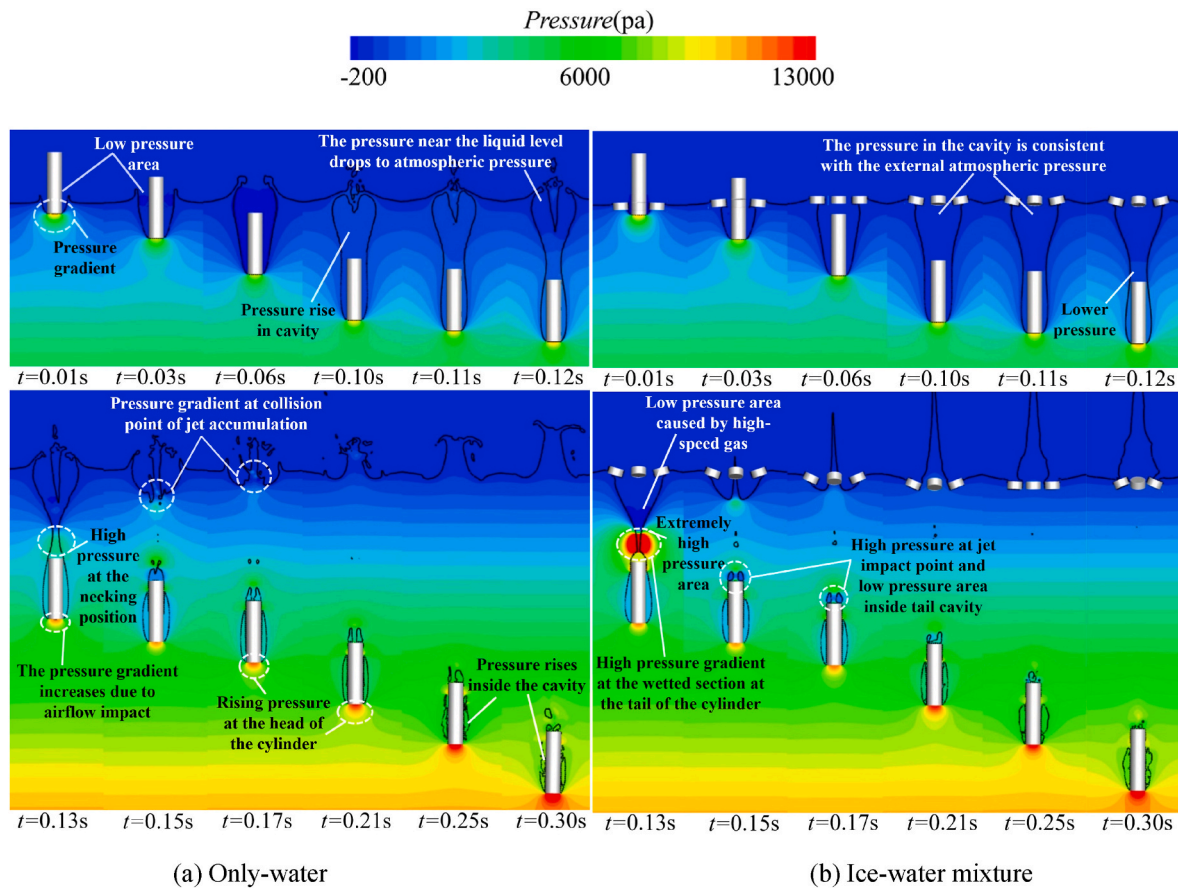From the cavity collapse stage (*t* = 0.15–0.30 s) shown in Fig. 19, it

Fig. 19. Pressure field distribution on the *xoy* section.

was found that in the only-water condition, the upward splashing jet generated by the deep closure carried a large amount of gas to the free surface at a high speed. Furthermore, it collided and coupled with the downward jet generated by the previous surface closure, resulting in a large area of pressure rise region. After coupling, the secondary splash was formed, and the high-pressure area near the water surface gradually disappeared after 0.21 s.

The downward high-speed moving jet affected the tail cavity and cylinder tail, which intensified the shedding of the cavity and changes in the motion characteristics of the cylinder. Between 0.21 and 0.30 s, the internal pressure of the attached cavity increased gradually as the cylinder deepened into water. When the internal pressure of the cavity was nearly consistent with the external environmental pressure of the current water depth, the instability fluctuation occurred and the cavity collapsed.

In the ice-water mixture condition, the pressure field distribution in the cavity collapse stage was almost consistent with that in the only-water condition, except for the jet with higher velocity impacting on the tail of the cylinder at 0.17 s, which caused the pressure at the impact point to be higher, resulting in an obvious low-pressure area inside the tail cavity and a relatively intense upward splashing jet. Therefore, the width of the pressure rise area below the free liquid surface was wider, and the pressure gradient was larger.

3.2.3. Unsteady vortex structure distribution characteristics

The complex motion state of the fluid can be reflected through vortices of different scales and intensities distributed in space. According to the "tendon of fluid motion" (Küchemann, 1965), vortices are important features that can accurately and effectively reflect the changes in the structural characteristics of the flow field. The in-depth analysis of the structural characteristics of the unsteady vortices in the

evolution of the cavity is highly significant for determining the influence mechanism of the floating ice on the structural characteristics of the flow field after entering the water of the cylinder.

Q criterion can effectively identify the position and intensity of vortex (Hunt et al., 1988). The second invariant *Q* of velocity gradient tensor based on Galilean invariance is defined by Haller (1999):

$$Q = \frac{1}{2}\left(\omega_{ij}\omega_{ij} - S_{ij}S_{ij}\right) \tag{12}$$

where $\omega_{ij} = \frac{\partial u_i}{\partial x_j} - \frac{\partial u_j}{\partial x_i}$ and $S_{ij} = \frac{1}{2}\left(\frac{\partial u_i}{\partial x_j} + \frac{\partial u_j}{\partial x_i}\right)$ are the rotation tensor and symmetric strain rate tensor, respectively.

When $Q > 0$, the rotation trend of the region is greater than the axial deformation, resulting in vortex. Else, the deformation rate is greater than the rotation rate, and the flow field in this region is mainly affected by shear deformation.

Fig. 20 shows the distribution of the *Q*-value in the *xoy* section at different moments in the two conditions. The red expression is $Q > 0$ and the blue expression is $Q < 0$. In the entire process of the cylinder entering the water, the evolution of the cavity is accompanied by a large number of complex vortex structures. The development, coupling, motion, separation, and dissipation of vortices can lead to changes in the flow field structure characteristics, which makes the interaction between cavity and turbulence more complex. The vortex structure is represented by the *Q* standard, which is based on the Euler method, and the dynamic characteristics of the vortex structure are summarised and analysed in combination with the velocity vector field in section 3.2.1.

In the initial water entry impact stage of the only-water condition, the negative *Q*-value was mainly concentrated around the head and tail of the cylinder and occupied most of the area, which indicated that the flow field was mainly affected by shear, and that the deformation effect
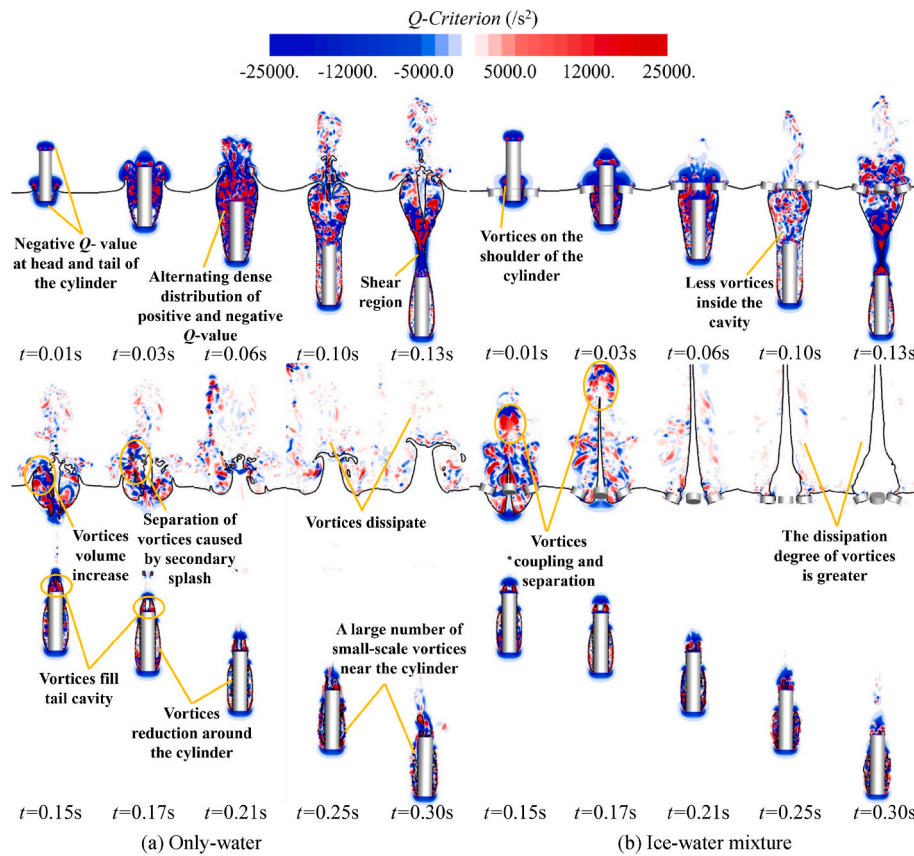
Fig. 20. Distribution of the *Q*-value on the *xoy* section.

was more prominent during this period. The positive *Q*-value only existed around the boundary of the initial cavity wall and the cylinder tail, and the directions of the vortices on both sides of the cylinder were opposite. In the ice-water mixture condition, the air entering the cavity hit the floating ice and rebounded to the cylinder wall. After friction with the wall, vortices are formed, causing positive *Q*-value to appear on the shoulder of the cylinder.

In the open cavity stage of the only-water condition ($t = 0.01$–0.06 s), a large number of vortices appeared near the splash and inside the cavity, and the positive and negative *Q*-value regions were alternately and densely distributed. Compared to the initial water entry stage, a larger area of multi-scale vortices was formed, indicating that the flow became more complicated during the expansion and development of the cavity, and that the rotation effect and shear deformation effects were present in the entire flow area. Furthermore, the liquid splashing caused the air flow field above the free surface to form vortices and gradually develop upward. Due to the floating ice, the vortices intensity of the flow field above the free surface in the ice-water mixture condition was weak, and the region remained affected by shear deformation.

Before and after entering the water for 0.10 s, the cavity development was relatively stable. The absolute value of positive and negative *Q*-values in the cavity, as well as the vortices strength and deformation strength decreased. The vortices above the free surface flowed far away and gradually weakened. The cavity necking phenomenon ($t = 0.13$ s) caused significant changes in the vortices dynamic characteristics of the entire flow field. The violent interaction between the liquid and cavity caused the area of the negative *Q*-value area in the necking section of the cavity to increase rapidly, resulting in a shear area like "bands". The compressed air moved to both sides at a high speed, thereby causing the volume and strength of the vortices near the free surface and around the cylinder to increase sharply. In the only-water condition, the flow field above the deep closure point became extremely complex under the

influence of the downward jet generated by previous surface closure, and a large number of vortices with different rotation directions and positions appeared. As the jet formed by deep closure moved to the liquid surface, the vortices also rose, and the volume gradually increased.

In the condition of ice-water mixture, the number of vortices was less at 0.10 s. The jet position generated by the deep closure had always been maintained on the axis of the cylinder, and the vortices position symmetry formed on both sides of the jet was excellent. In both conditions, the large area inside the tail cavity formed after deep closure was positive *Q*-value, which indicated the presence of vortices inside the tail cavity after its formation. As the water entry time increased, a large baroclinic torque generated by the secondary splash impact, which promoted the expansion of a large number of vortices regions. Owing to the mutual stretching mechanism of the vortices, the vortices coupled continuously and separated during the upward movement. However, the vortices around the cylinder gradually decreased, only existed around the head and shoulder of the cylinder ($t = 0.21$ s).

Cavity collapse occurred as the cylinder went deeper, and the surrounding flow field was extremely complex. The positive and negative *Q*-value areas near the tail cavity and the attached cavity increased and interlaced, and a large number of small-scale vortices appeared. The vortices with a certain scale carried energy to impact the surface of the attached cavity to deform it, and the collision coupling between the vortices resulted in cavity breakage. The rotation and deformation effects jointly dominated the cavity collapse process.

The *Q*-value of the vortices above the free surface decreased continuously until the vortices disappeared. There could be two reasons for the large-area dissipation of the vortices above the free surface. First, the secondary splash weakened and fell back after reaching its peak value, which no longer provided energy for the flow of the air field. Second, energy was continuously consumed during the vortices

movement, which decreased the intensity. The vortices dissipation above the free surface in the ice-water mixture condition was much greater, and vortices were barely observed at 0.30 s.

During the process of entering the water, gas continuously flowed into and out of the cavity. The complex flow field inside the cavity and near the free surface exhibited high-velocity gradients and pressure gradients, which resulted in the formation of a large number of unsteady vortices. Considering the distribution of Q-value in the plane section is not enough to fully reflect the changes in the three-dimensional characteristics of vortices, the vortices characteristics are supplemented based on the iso-surface of $Q = 40000 s^{-2}$, as shown in Fig. 21.

In the initial impact stage of water entry, vortices stretched and baroclinic torque dominated the flow field, and large amounts of air flowed into the initial cavity at a high speed, which resulted in a high-velocity gradient around the tail and shoulder of the cylinder (Fig. 15), thus forming two vortex rings connected with the head and tail (Fig. 21a). The vortex rings were parallel to the tail plane of the cylinder and symmetrically distributed around the axis of the cylinder. However, only one vortex ring appeared at the tail of the cylinder in the ice-water mixture condition, (Fig. 21b). As shown in Fig. 15, owing to the influence of floating ice, the velocity of the surrounding flow field was relatively low around the tail of the cylinder during the initial impact stage, which was insufficient to provide the high-velocity gradient for the formation of the vortex ring. Moreover, owing to the rebound reflection between the cylinder and floating ice when the external air flowed in, a large number of small-scale vortices formed during the friction with the wall.

In the open cavity stage, the vortex ring gradually dissipated and disappeared under the action of flow impact, and the vortices in the flow field around the cylinder moved continuously with the evolution of cavity. Under the condition of ice-water mixture, the jet exhibited a small volume and a fast speed, which resulted in the formation of vortices around the jet, and moved rapidly to the far field. Additionally, the downward jet was not formed owing to the absence of surface closure, and the number and intensity of vortices in the cavity decayed rapidly. On comparing Fig. 21a and Fig. 21b, it could been seen that the number of vortices at 0.10 s was much less than that of only-water condition.

Due to the complicated changes in the flow field caused by the high-speed airflow before and after deep closure, a large number of new vortices formed. The necking degree of the ice-water mixture condition was severe, causing the flow velocity of the jet generated by deep closure to be higher (Fig. 16). The velocity gradient around the tail of the cylinder was relatively larger, and a small vortex ring had formed at this position. In the cavity collapse stage ($t = 0.15$–0.30 s), the number and intensity of vortices around the cylinder decreased, then increased, and decreased again, thereby forming a strong interaction with the surrounding flow field and cylinder wall. This confirmed that the development of the vortex structure was closely related to the evolution of the cavity. In summary, the floating ice caused significant changes to the velocity gradient and pressure gradient around the cylinder during the entire process of the cavity entering the water, which has an important impact on the generation and development of vortices.

3.3. Influence of ice-water mixture on the fluid hydrodynamic and motion characteristics of the cylinder and floating ice

Changes in motion characteristics such as acceleration and velocity were closely related to the hydrodynamic characteristics in the process of water entry. The floating ice appeared overturned and diffused under fluid force. Based on the 0.5 D_0 floating ice thickness in the above analysis, the conditions with floating ice thicknesses of 0.25 D_0, 0.75 D_0 and 1.0 D_0 were established. The motion states of floating ice with different thicknesses in the water entry process were compared and analysed, and the influence of ice-water mixture with different ice thicknesses on the motion and fluid hydrodynamic characteristics of the cylinder was analysed in depth.

3.3.1. Variation characteristics of the motion attitude of floating ice with different thicknesses

Because the positions of the four floating ice bodies were evenly distributed around the water entry point and the motion attitude of each floating ice body was approximately the same, we only analysed the motion state of the floating ice in the y direction of the water entry point.
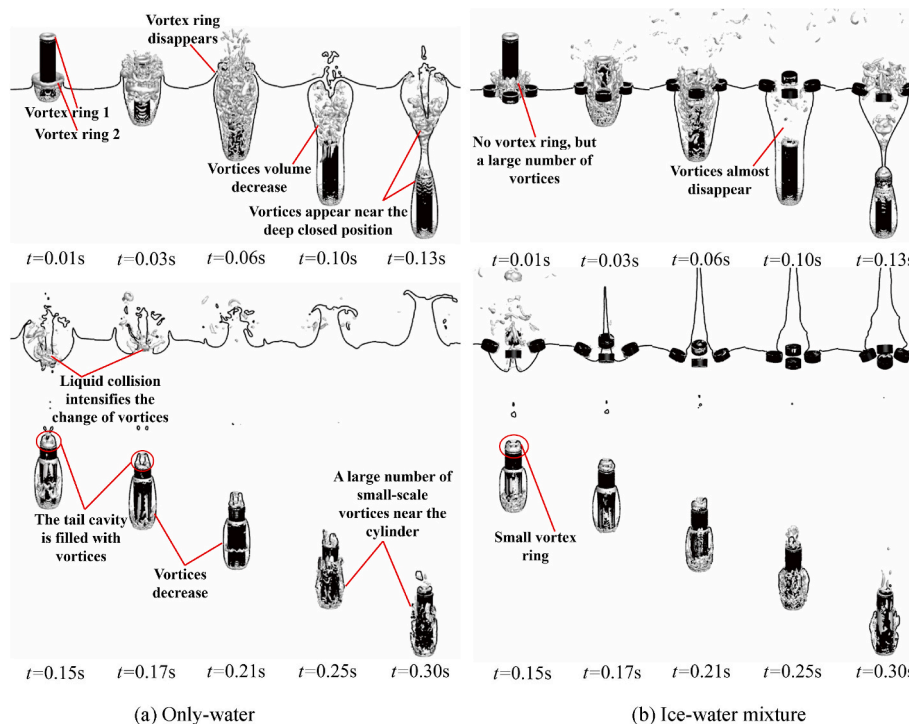

(a) Only-water

(b) Ice-water mixture

Fig. 21. Vortices in three-dimensional spatial distribution.

(a) Overturning angle
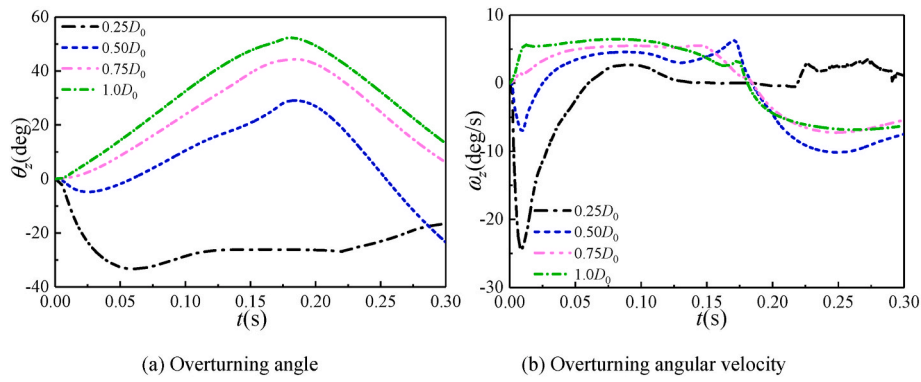
(b) Overturning angular velocity

Fig. 22. Variation of motion attitude of the floating ice with different thicknesses.

Fig. 22 shows the curves of the overturning angle and the overturning angular velocity of the floating ice around the z-axis after entering the water of the cylinder, respectively. The anti-clockwise rotation (inward overturning) around the z-axis is defined as the positive direction.

For ice thicknesses of 0.75 D_0 and 1.0 D_0, the overturning angle and angular velocity exhibited the same change trend as for the other time periods, except that a slight difference was observed in the initial water entry impact stage and cavity closure stage. The floating ice first flipped inward, then rotated outward, and finally approached the horizontal position at 0.3 s. The floating ice with a thickness of 0.5 D_0 first weakly flipped outward in the initial water entry impact stage, and then turned outward after turning inward in the open cavity stage. Finally, the direction of rotation became negative at 0.3 s. On comparing the motion attitude curves of the floating ice with the above three thicknesses, we observed that the maximum overturning degree of the floating ice increased as the ice body thickness increased, owing to the difference in the fluid force. Because the thicker floating ice had a larger volume submerged in the water, and the surrounding fluid had a larger area of action on the floating ice during the process of the cylinder entering the

water. The larger ratio of the fluid force to the inertial force of the floating ice itself, the greater the degree of influence on the overturning attitude of the floating ice.

The floating ice with a thickness of 0.25 D_0 maintained the attitude of turning to the outside during the water entry process, and the overturning angular velocity peak appeared in the initial water entry stage, indicating that when the ice thickness was less than a critical value, the floating ice was mainly affected by the impact of the initial splashing fluid and hence showed a completely different motion attitude from the floating ice with a thickness greater than the critical value in the subsequent period.

Fig. 23 shows the variation of velocity and displacement of floating ice in the vertical and horizontal directions, respectively, wherein the vertical downward direction is the positive direction. The change degree of the vertical velocity and vertical displacement both decreased as the ice thickness increased, indicating a consistent change trend. However, the change degree of horizontal velocity increased as the ice thickness increased, and the horizontal displacement decreased as the ice thickness increased only when greater than 0.5 D_0. The variation trend of the

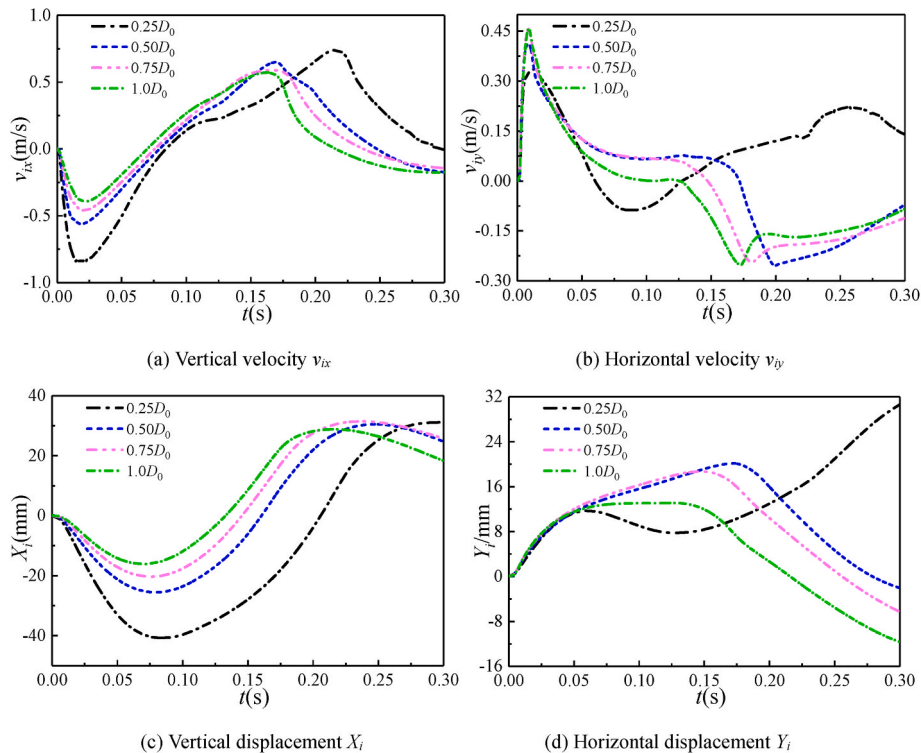

(a) Vertical velocity v_{ix}

(b) Horizontal velocity v_{iy}

(c) Vertical displacement X_i

(d) Horizontal displacement Y_i

Fig. 23. Velocity and displacement of the floating ice with different thicknesses.

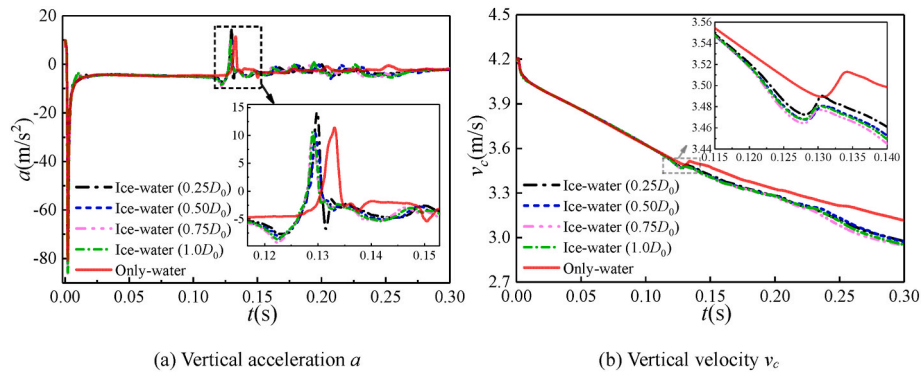(a) Vertical acceleration a (b) Vertical velocity v_c

Fig. 24. Acceleration and velocity time histories of water entry of the cylinder under different conditions.

horizontal velocity and displacement of the floating ice with the thickness of 0.25 D_0 in the open cavity stage and the subsequent period was opposite to that of the ice with other thicknesses, indicating that the horizontal motion state of the floating ice with a critical thickness as the boundary shows an opposite trend in the cavity development stage after the cylinder enters the water.

3.3.2. Motion characteristics of the cylinder

Fig. 24 shows the vertical acceleration and velocity curves of the cylinder under different conditions, respectively. Fig. 25 shows the evolution process of the cavity shape at 0.5 D_0 ice thickness condition between 0.123 and 0.135 s after the cylinder entered the water. The motion characteristics of the cylinder in the ice-water mixture and only-water conditions were significantly different in the cavity closure and collapse stages, whereas the change trend and amplitude of the cylinder acceleration in other time periods were basically the same. In the conditions of different ice thicknesses, the variation trend of cylinder motion characteristics was almost the same during the entire time period. However, when the ice thickness was 0.25 D_0, a slight difference was observed in the amplitude of acceleration and velocity curve of the cylinder in the cavity deep closure stage, indicating that the floating ice with different thicknesses had little effect on the motion trajectory of the cylinder after entering the water vertically. However, the existence of floating ice resulted in a large difference in the motion characteristics of the cylinder compared with only-water. In the following, the motion characteristics of the cylinder under ice-water mixture and only-water conditions with the ice body thickness of 0.5 D_0 were analysed.

Before the cylinder collided with the water surface, it made a free fall movement, which was only affected by gravity and the weak air resistance. At the collision moment, the speed decreased significantly in a very short time. After entering the water, the initial cavity was formed, the acceleration recovered rapidly, and the velocity decline rate gradually slowed down. Then, the cavity developed steadily. The acceleration of the cylinder remained stable and the velocity decreased evenly under the combined action of resistance and gravity.

After 0.12 s, the cavity evolution gradually transited to the necking and closure stage, and the acceleration and velocity curves of the two conditions began to show significant differences. As shown in Fig. 25b, between 0.12 and 0.129 s, the cavity diameter decreased rapidly in the ice-water mixture condition caused by the more severe necking due to the influence of floating ice. Before the deep closure of the cavity, the tail of the cylinder had been in contact with the cavity wall. The liquid in the wetted part exerted resistance on the cylinder tail, hindering the movement of the object. At this time, the acceleration curve slightly formed a downward bulge, and the velocity curve decreased rapidly. During this period, deep closure had not yet occurred in the cavity in the only-water condition, and the cylinder was still completely wrapped by the cavity without getting wet. Therefore, the acceleration and velocity curves under the only-water condition did not change (Fig. 25a).

Between 0.129 and 0.135 s, the cavity in the necking section of the ice-water mixture condition occurred deep closure, and the liquid impact point produced a high-pressure area. The force caused by the pressure difference between the head and tail of the cylinder was greater than that of the wet area at the head and tail. The cylinder reached a high acceleration in a short time and accelerated the downward movement. As the cylinder continued to enter the water, the force of liquid impacting the cylinder decreased, resulting in the decrease and reduction of the high-pressure area and the pressure value generated at the cylinder tail, thereby causing the acceleration to fall below 0 and the velocity to decay again.

As shown in Fig. 25a, the deep closure of the only-water condition occurred later. The cavity wall before 0.132 s barely wet the cylinder, and hence the acceleration and velocity of the cylinder were still relatively stable without mutation. Considering the necking degree was not as severe as that of the ice-water mixture condition, the pressure in the high-pressure zone was smaller, and the peak value of the instantaneous acceleration was slightly lower. However, because the necking process lasted longer than that of the ice-water mixture condition, the wetted area of the cylinder and the liquid obstruction were smaller, and the duration of the downward resultant force was longer, which increased
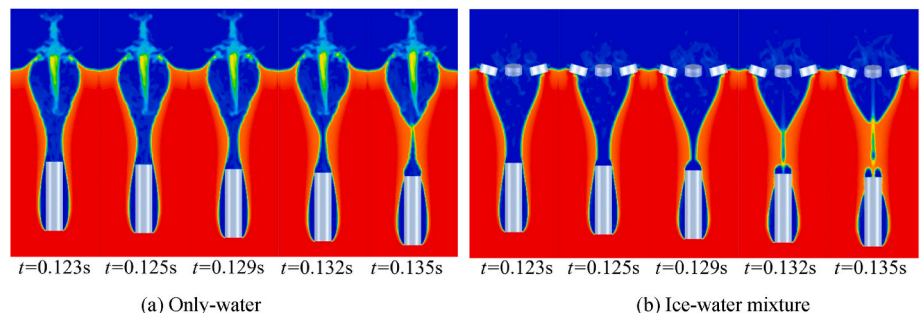

t=0.123s t=0.125s t=0.129s t=0.132s t=0.135s   t=0.123s t=0.125s t=0.129s t=0.132s t=0.135s

(a) Only-water   (b) Ice-water mixture

Fig. 25. Evolution process of the cavity shape between 0.123 and 0.135 s.

the speed, resulting in an obvious difference in the speed between the two conditions.

After the deep closure of the cavity, the acceleration of the partially wetted cylinder fluctuated due to complex factors such as the continuous impact of the jet on the cylinder and the falling of the tail cavity. Before the collapse of the attached cavity (0.15–0.25 s), the fluctuations of the acceleration curves of the two conditions were quite different, the fluctuation amplitude of the ice-water mixture condition was large but that of the only-water condition was weak. This can be attributed to the fact that the tail cavity of the ice-water mixture condition fell off quickly, and the floating ice exhibited a large disturbance to the cylinder.

Furthermore, the attached cavity collapsed (0.25–0.30 s), the pressure field around the cylinder was almost the same as the external environment, and the acceleration curves of the two conditions were almost the same. In all, the acceleration values of both conditions in the cavity collapse stage were slightly smaller than those of the open cavity stage because the length of the cavity was shortened after the cavity collapse, and the velocity of the cylinder was lower than that of the open cavity stage, which decreased the resistance.

4. Conclusions

In this study, we compared and analysed the process of a cylinder entering the only-water and ice-water mixture vertically at a low speed by conducting numerical simulations. We investigated the influence law of floating ice on the evolution of the cavity shape, structural characteristics of the flow fields, cylinder motion, and variations in the fluid hydrodynamic characteristics after entering the water in each stage. The main findings of this study are summarised as follows:

(1) As the cylinder passes through the ice-water mixture, the floating ice causes changes to the cavity shape and pressure difference between the inside and outside the cavity by hindering the liquid diffusion, contraction, and retraction, which significantly influences the cavity closure and collapse stage. As a result, it changes the motion and hydrodynamic characteristics of the cylinder in the process of entering the water. However, the motion attitude of floating ice significantly changes according to its thickness. Although different thicknesses of floating ice have little effect on the motion characteristics of the cylinder after vertical water entry, the existence of floating ice results in a large difference in the motion characteristics of the cylinder compared with the case of no floating ice.

(2) As the cylinder passes through the ice-water mixture, the floating ice hinders the development of the splash and changes the splash form, which makes the cavity expand slower and the opening duration of the cavity mouth be longer than that of only-water with the failure to form surface closure. Moreover, deep closure occurs earlier in the ice-water mixture environment, the volume of the tail cavity and attached cavity is smaller, the wetness degree of the cylinder is higher compared with that of the only-water environment, the shedding speed of the tail cavity is faster, and the evolution of cavity shape is significantly different.

(3) The flow field structures of the cylinder after entering the water are significantly different in the only-water and ice-water mixture. Pertaining to the velocity field distribution, the amplitude and fluctuation of air velocity within the cavity are quite different. Pertaining to the pressure field distribution, owing to the failure of forming surface closure during the process of passing through the ice-water mixture, the pressure difference inside and outside the cavity is large, and the severity of necking is stronger than that of only-water environment, which intensifies the shedding of the tail cavity and changes in the motion characteristics of the cylinder. Pertaining to the distribution of unsteady vortex structure, during the water entry impact stage, the flow field is mainly affected by shear, and the deformation effect

is prominent. During the subsequent development of the open cavity, the rotation effect and shear deformation effect fill the entire flow region together. The most interesting finding is that there are two vortex rings appear at the tail and shoulder of the cylinder, respectively, during the initial stage of the water entry for only-water. However, there is only one vortex ring appears at the tail of the cylinder for the ice-water mixture, but after the deep closure, another smaller vortex ring is generated at the cylinder tail.

(4) The cylinder motion and hydrodynamic characteristics in the only-water and ice-water mixture environments begin to show differences at the cavity closure stage. In the ice-water mixture environment, the acceleration and velocity fluctuations of the cylinder appear earlier, and the fluctuation range is larger owing to the severer necking. The degree of wetness and the impact on the cylinder caused by the deep closure are larger, which leads to a more obvious difference in the cylinder velocity of the two environments after the deep closure is finished.

CRediT authorship contribution statement

Hao Wang: Investigation, Conceptualization, Methodology, Software, Writing – original draft, Writing – review & editing. **Yuchuan Luo:** Investigation, Data curation, Validation. **Zhihua Chen:** Conceptualization, Supervision, Visualization. **Zeqing Guo:** Software, Data curation. **Zhengui Huang:** Formal analysis, Writing – review & editing.

Declaration of competing interest

The authors declare that they have no known competing financial interests or personal relationships that could have appeared to influence the work reported in this paper.

Acknowledgments

References

Cai, X.W., Xuan, J.M., Wang, B.S., Li, W., Zhang, J., 2020. Numerical simulation of thin body passing through the ice-water mixture flow field. Acta Armamentarii 41 (S1), 79–90.

Chen, T.T., Chen, X.E., 2021. Numerical simulation of sea ice in Bohai Sea in winter in 2012—2013. J. Oceanol. Limnol. 43, 1–10.

Gekle, S., Gordillo, J.M., van der Meer, R.M., Lohse, D., 2009. High-speed jet formation after solid object impact. Phys. Rev. Lett. 345, 1–4. https://doi.org/10.1103/PhysRevLett.102.034502.

Gekle, S., Peters, I.R., Gordillo, J.M., van der Meer, R.M., Lohse, D., 2010. Supersonic air flow due to solid-liquid impact. Phys. Rev. Lett. 104, 24501. https://doi.org/10.1103/PhysRevLett.104.024501.

Haller, G., 1999. An objective definition of a vortex. J. Fluid Mech. 525, 1–26. https://doi.org/10.1017/S0022112004002526.

He, C.T., Wang, C., He, Q.K., Q, Y., 2012a. Low speed of water-entry of cylindrical projectile. Atca Phys. Sin. 61, 1–8.

He, C.T., Wang, C., Wei, Y.J., Ma, X.F., 2012b. Vertical water entry cavity of cylinder body. Beijing Hangkong Hangtian Daxue Xuebao/J. 38, 1542–1546.

Hou, Z., Sun, T.Z., Quan, X.B., Zhang, G.Y., Sun, Z., Zong, Z., 2018. Large eddy simulation and experimental investigation on the cavity dynamics and vortex evolution for oblique water entry of a cylinder. Appl. Ocean Res. 81, 76–92. https://doi.org/10.1016/j.apor.2018.10.008.

Huang, Z.G., Wang, R.Q., Chen, Z.H., Hou, Y., Luo, Y.C., 2018. Experimental study of cavity characteristic induced by vertical water entry impact of a projectile with a 90° cone-shaped head at different velocities. Combust. Explos. Shock Waves 38, 1189–1199. https://doi.org/10.11883/bzycj-2018-0115.

Hunt, J.C.R., Wray, A.A., Moin, P., 1988. Eddies, streams, and convergence zones in turbulent flows. In: Studying Turbulence Using Numerical Simulation Databases, vol. 2.

Iranmanesh, A., Passandideh-Fard, M., 2017. A three-dimensional numerical approach on water entry of a horizontal circular cylinder using the volume of fluid technique. Ocean Eng 130, 557–566. https://doi.org/10.1016/j.oceaneng.2016.12.018.

Jiang, Y.H., Xu, S.L., Zhou, J., 2017. Water entry experiment of a cylindrical vehicle with disc cavitator. J. Eng. Mech. 34, 241–246. https://doi.org/10.6052/j.issn.1000-4750.2015.09.0726.

Korobkin, A.A., Scolan, Y.M., 2006. Three-dimensional theory of water impact. Part 2. Linearized Wagner problem. J. Fluid Mech. 549, 343–373. https://doi.org/10.1017/S0022112005008049.

Küchemann, D., 1965. Report on the I.U.T.A.M. symposium on concentrated vortex motions in fluids. J. Fluid Mech. 21, 1–20. https://doi.org/10.1017/S0022112065000010.

Li, P.X., 2009. Dominant climate factors influencing the arctic runoff and association between the runoff and arctic sea ice. Hai Yang Xue Bao 29, 10–20. https://doi.org/10.1007/s13131-010-0058-3.

Liu, H., Zhou, B., Han, X.S., Zhang, T., Zhou, B.K., Gho, W.M., 2020. Numerical simulation of water entry of an inclined cylinder. Ocean Eng 215, 107908. https://doi.org/10.1016/j.oceaneng.2020.107908.

Logvinovich, G.V., 1969. Hydrodynamics of Flows with Free Boundaries. Naukova Dumka, Kiev.

Luo, Y.C., Huang, Z.G., Gao, J.G., Chen, Z.H., Hou, Y., Guo, Z.Q., 2019. Experiment research of low-speed oblique water-entry of truncated cone-shaped projectile. Combust. Explos. Shock Waves 39, 80–87. https://doi.org/10.11883/bzycj-2018-0498.

Ma, Q.P., He, C.T., Wang, C., Wei, Y.J., Lu, Z.L., Sun, J., 2014. Experimental investigation on vertical water-entry cavity of sphere. Combust. Explos. Shock Waves 34, 174–180. https://doi.org/10.11883/1001-1455(2014)02-0174-07.

Menter, F.R., 1993. Zonal Two Equation K-ωTurbulence Models for Aerodynamic Flows. Nasa Sti/recon Technical Report N, pp. 93–2906. https://doi.org/10.2514/6.1993-2906.

Nam, J., Park, I., Lee, H.J., Kwon, M.O., Choi, K., Seo, Y., 2013. Simulation of Optimal Arctic Routes using a numerical Sea Ice model based on an ice-coupled ocean circulation method. Int. J. Nav. Arch. Ocean. 5, 210–226. https://doi.org/10.2478/IJNAOE-2013-0128.

Nguyen, V.T., Phan, T.H., Park, W.G., 2020. Modeling and numerical simulation of ricochet and penetration of water entry bodies using an efficient free surface model. Int. J. Mech. Sci. 182, 105726. https://doi.org/10.1016/j.ijmecsci.2020.105726.

Nguyen, V.T., Phan, T.H., Duy, T.N., Park, W.G., 2021. 3D simulation of water entry of an oblique cylinder with six-degree-of-freedom motions using an efficient free surface flow model. Ocean Eng 220, 108409. https://doi.org/10.1016/j.oceaneng.2020.108409.

Scolan, Y.M., Korobkin, A., 2001. Three-dimensional theory of water impact. Part 1. Inverse wagner problem. J. Fluid Mech. 440, 293–326. https://doi.org/10.1017/S002211200100475X.

Techet, A.H., Truscott, T.T., 2011. Water entry of spinning hydrophobic and hydrophilic spheres. J. Fluids Struct. 27, 716–726. https://doi.org/10.1016/j.jfluidstructs.2011.03.014.

Truscott, T.T., Epps, B.P., Belden, J., 2014. Water entry of projectiles. Annu. Rev. Fluid Mech. 46, 355–378. https://doi.org/10.1146/annurev-fluid-011212-140753.

Truscott, T.T., Techet, A.H., 2009. Water entry of spinning spheres. J. Fluid Mech. 625, 135–165. https://doi.org/10.1017/S0022112008005533.

Wang, R.Q., Huang, Z.G., Guo, Z.Q., Chen, Z.H., Gao, J.G., Hou, Y., 2017. Experimental study of low speed vertical water entry with different head shape projectiles. J. China Ordnance 38, 45–50. https://doi.org/10.12783/ballistics2017/16776.

Worthington, A.M., Cole, R.S., 1897. Impact with a liquid surface studied by the aid of instantaneous photography. Philos. T. R. Soc. A 189, 137–148. https://doi.org/10.1098/rsta.1897.0005.

Zhang, J., Cai, X.W., Xuan, J.M., Wang, Y.L., 2020. Numerical simulation of flow field of projectile passing through ice water mixture. Dandao Xuebao/J. 32, 35–40.